REDUCTION OF p-NITROPHENOL TO p-AMINOPHENOL BY USING NiO CATALYSTS: A COMPARATIVE STUDY

R. S. Sutar,[a] R. P. Barkul[a] and M. K. Patil[a]*

Keywords: nickel oxide; p-nitrophenol reduction; sodium dodecyl sulfate; p-aminophenol.

Different nickel oxide catalysts have been prepared by simple precipitation method using different nickel precursors and using surfactant sodium dodecyl sulfate (SDS) or without surfactant. The prepared catalysts have been characterized by using XRD and FT-IR. The particle sizes have been calculated by using the Scherrer equation. The nickel oxide catalyst prepared by using nickel acetate as precursor and surfactant SDS has shown less particle size as compared to other catalysts prepared by using other precursors. Also, nickel oxide catalyst prepared using nickel acetate precursor and surfactant SDS has shown higher catalytic activity for reduction of p-nitrophenol (PNP) to p-aminophenol (PAP) using sodium borohydride ($NaBH_4$). Also, for the said reaction effect of concentration of p-nitrophenol on catalytic efficiency has been studied.

* Corresponding Authors
E-Mail: meghshyam_patil@yahoo.com
[a] Department of Chemistry, Dr. Babasaheb Ambedkar Marathwada University, Aurangabad, Sub-campus Osmanabad- 413 501, MS, India

Introduction

Countless chemical protocols have been depended upon the catalysis, and the catalysts play a crucial role in the production and manufacture of chemicals and materials because catalytic reactions generally occur under milder conditions compared to the noncatalytic reactions.[1,2,3] The use of heterogeneous catalysts is one of the best attractive alternatives for synthetic strategies and adopted by organic chemists for increasing the efficiency of a wide range of organic reactions.[4]

Recently, transition metal oxides as catalysts are to tailor and design according to their sizes, structure in nanodimensions and therefore their surface chemistry and catalytic properties.[5-9] An increasing number of illustrations are accessible in the literature where nickel-based nanoparticles have been used as catalysts during organic transformations.[10,11]

Nickel oxide (NiO) is a p-type semiconductor material with magnetic power and wide band-gap energy (3.6-4.0 eV). It has been exploited in many different areas such as gas sensing, biomedicinal, electrochemical, supercapacitors, photovoltaic devices, memory storage, fuel cells, conducting materials, and electrode materials.[12] Also, NiO nanoparticles have been used as heterogeneous catalysts for various organic transformations.[13-16] The nanoparticulate NiO catalysts have shown an edge over the bulk NiO catalysts since they have a higher surface to volume ratios.[17] NiO nanoparticles have been synthesized by various routes such as chemical precipitation method, microemulsion, electron spray synthesis, laser ablation, and hydrothermal method.[18,19]

Arylamines are useful raw materials for several industries such as for the synthesizing rubbers, paints, plastics and pharmaceutically significant value-added products. The wide commercial use of arylamines has led to the improvement of new and efficient protocols for the reduction of nitroarenes. The reduction of nitroarenes with sodium borohydride is one of the most simple, cleanest and most accepted methods, but the very slow hydrolysis of sodium borohydride makes this method unusable[20,21] until some catalyst is used.

In this work, we have been prepared NiO nanomaterials by simple precipitation method (with and without surfactant) using two different precursors (nickel acetate and nickel nitrate). Prepared catalysts were characterized by XRD, FT-IR and applied for catalytic reduction of p-nitrophenol to p-aminophenol.**es:**

Experimental

The main starting materials were nickel(II) acetate, nickel(II) nitrate hexahydrate, sodium hydroxide (NaOH), sodium dodecyl sulfate (SDS) and ethanol, all of them were analytical grade and purchased from Kemphasol and Sigma-Aldrich. These chemicals were used as received without further purification.

Synthesis of NiO nanoparticles

In this preparation, we have prepared two separate solutions; a solution of 16.65 g of nickel acetate in 83.25 mL of deionized water, and a solution of 10 g sodium hydroxide in 250 ml of deionized water. Amount of 6.34 g of surfactant sodium dodecyl sulfate has been added to above-mentioned nickel acetate solution with continuous stirring. Next, the prepared sodium hydroxide solution was added dropwise with constant stirring to the solution of nickel acetate and surfactant. The mixed solution was stirred by a magnetic stirrer at room temperature for 1 h. The resultant light-green solution was kept at room temperature for settle down. The formed precipitate was then filtered, washed with deionized water several times and dried at 50ºC for 24 hours. Finally, the obtained powder has been calcined at 500ºC for 4 hrs. The

catalyst is abbreviated as NiAC-SDS. By adopting a similar protocol, we have synthesized NiO nanoparticles by using nickel acetate as precursor without using surfactant and abbreviated as NiAC. Furthermore, we have prepared NiO nanoparticles by using nickel nitrate as a precursor, SDS as a surfactant and without surfactant. These catalysts are abbreviated as NiNT-SDS and NiNT respectively.

Characterization

X-ray diffraction analysis of prepared catalysts has been carried using X-ray diffractometer (Bruker) with CuK_{α} irradiation at 40 kV and 40 mA. Phase identification of the nickel oxide was performed. Furthermore, FT-IR analysis has been conducted on Thermo Nicolet Nexus 670 spectrometer in the range 4000 to 400 cm^{-1}.

Conversion of p-nitrophenol to p-aminophenol

Firstly, p-nitrophenol (10 mg) was dissolved in 100 ml distilled water, the reaction mixture was kept for stirring for 1 h. The reducing agent sodium borohydride was added to the solution of p-nitrophenol in a round bottom flask and stirred for 30 min. After that 30 mg prepared NiO catalyst was added. The UV-visible spectra have been taken for samples collected after a different time interval from the reaction mixture. The various experiments of reduction of p-nitro phenol have been carried out by varying p-nitrophenol concentration.

Results and Discussions

X-Ray diffraction analysis

XRD was used for the identification of phase and size of NiO material and also gives information on unit cell dimensions. The Figure 1 shows the XRD pattern of NiO catalyst exhibited five XRD peaks at 2θ 37.1°, 43.3°, 62.9°, 75.2° and 79.2°, corresponding to the (101), (012), (110), (113) and (202) planes, respectively of cubic NiO (JCPDS44-1159).[29]

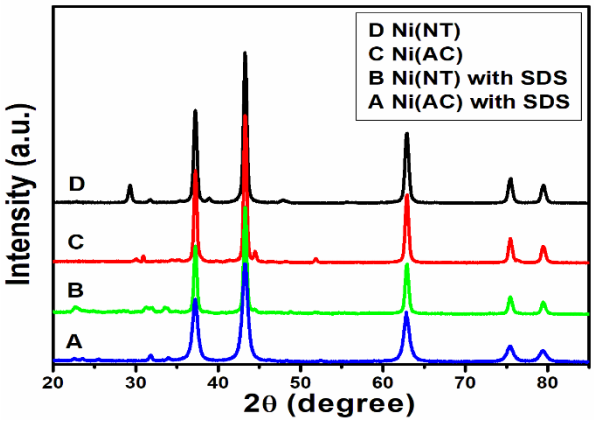

Figure 1. XRD pattern of NiO catalyst.

The particle size of the nanoparticles was calculated through the Scherrer's equation.[30]

$$[D = k\lambda/\beta\cos\theta]$$

where D is the average crystallite domain size perpendicular to the reflecting planes, k is the constant, λ is the wavelength, β is the full width at half maximum and θ is the diffraction angle. The calculated average crystallite size of NiAC-SDS, NiAC, NiNT-SDS and NiNT are 11.76 nm, 19.23 nm, 20.08 nm and 21.55 nm, respectively.

FT-IR analysis

Figure 2 shows the FT-IR spectrum of the NiO catalyst (NiAC-SDS). The broad absorption band centered at 3319 cm^{-1} is attributed due to the band O–H stretching vibrations, and the band at 1619 cm^{-1} is attributed due to bending mode of H–O–H.

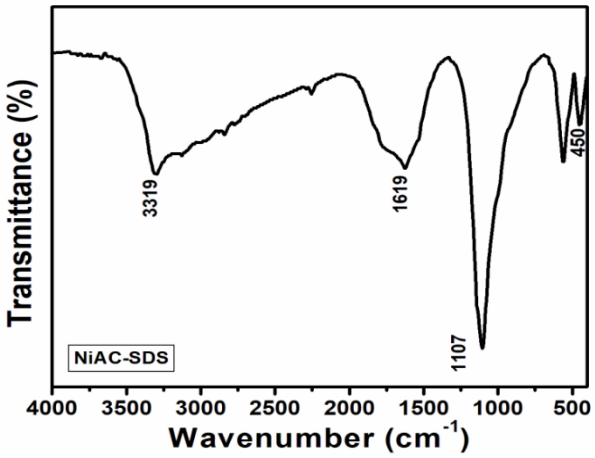

Figure 2. FT-IR spectrum of NiO catalyst (NiAC-SDS)

The band at 1107 cm^{-1} is due to the fact that the calcined powder tends to absorb water and carbonate ion physically. The weak band at 450 cm^{-1}corresponds to the bending vibration of metal oxide (Ni-O) bond.

Catalytic reduction of p-nitrophenol

Figure 3 shows the conversion of p-nitrophenol to p-aminophenol (Scheme 1) using sodium borohydride (10 mg) and the different catalysts. p-Nitrophenol having λ_{max} at ~320 nm. After the addition of sodium borohydride, λ_{max} was shifted from ~320 nm to 400 nm due to formation of p-nitrophenolate ion. After the addition of catalysts, the intensity of the band at 400 nm starts decreasing and new band will appear at 300 nm which is attributed to the formation of p-aminophenol. The initial color of p-nitrophenol is light yellow, becomes intense yellow on the addition of $NaBH_4$ (due to the formation of p-nitrophenolate ion) and after addition of a catalyst, the intensity of yellow color decreases.

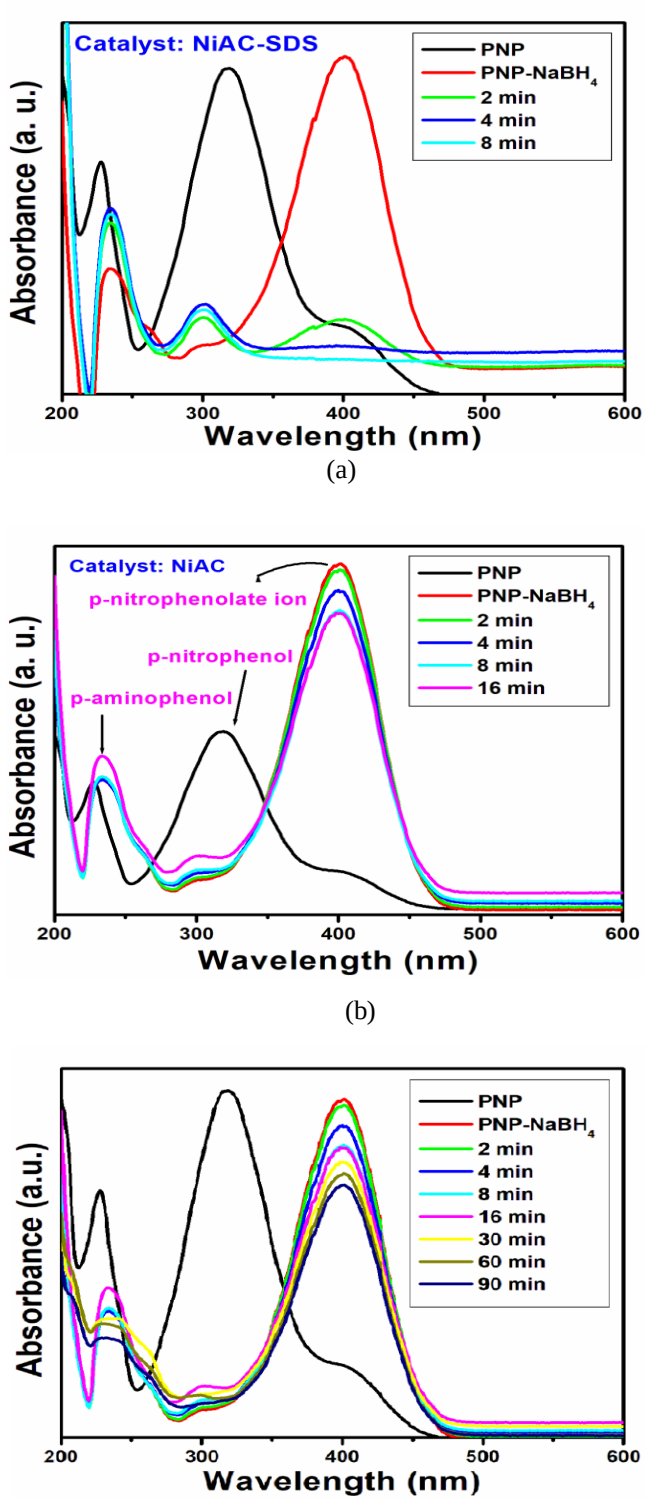

Figure 3. Conversion of PNP to PAP using catalysts a) NiAC-SDS, b) NiAC, c) NiNT-SDS.

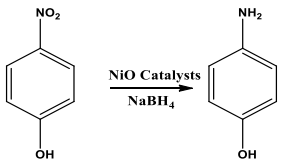

Scheme 1. Conversion of p-nitrophenol to p-aminophenol

From Figure 3 among the four NiO catalysts prepared, the NiAC-SDS have considerably good activity for this reaction than other catalysts. We have carried out further study, by using NiAC-SDS catalyst.

Effect of concentration of p-nitrophenol

On increasing the concentration of p-nitrophenol, the rate of conversion to p-aminophenol decreases (Figure 4). It is due to a decrease in active sites of the catalysts as compared to a number of molecules of p-nitrophenol.

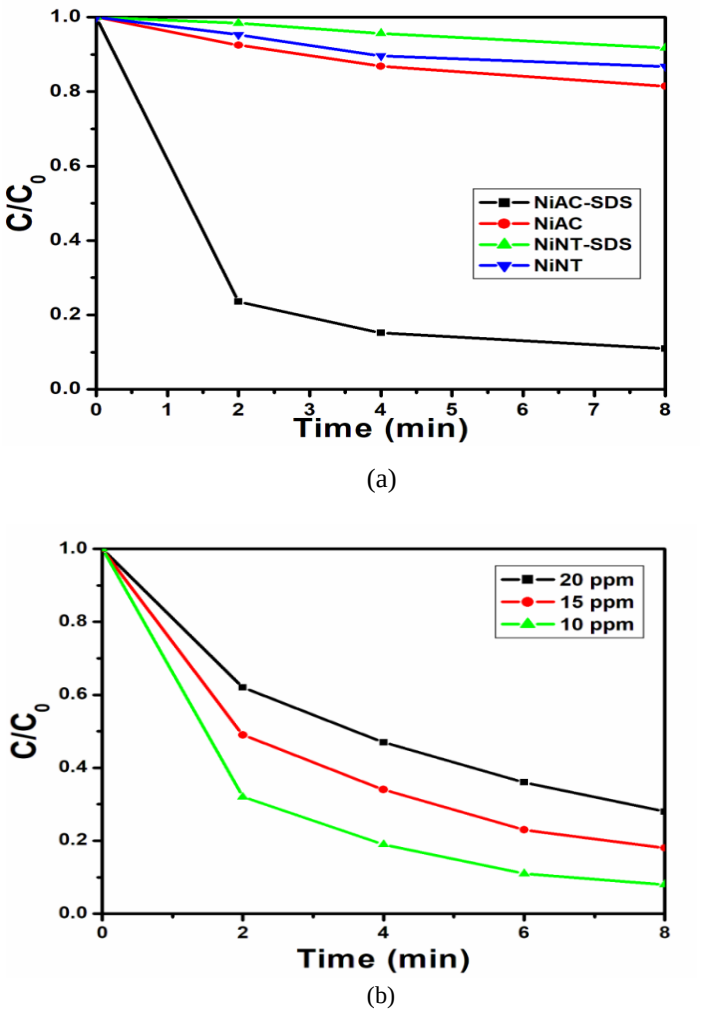

Figure 4. Kinetical parameters of PNP conversion into PAP using various catalysts (a) and the effect of p-nitrophenol concentration with using NiAC-SDS catalyst

Conclusions

We have successfully synthesized the NiO material by using a simple precipitation method and prepared catalysts having crystallite size on the nanometer scale. From the XRD analysis, NiO catalyst prepared by using acetate precursor and sodium dodecyl sulfate as surfactant have shown crystalline size 11.76 nm and formation of cubic phase. Furthermore, this catalyst has shown better catalytic activity for the conversion of p-nitrophenol to p-aminophenol.

Acknowledgment

RSS thanks the University Grants Commission (UGC), New Delhi, India for a Senior Research Fellowship.

This paper was presented at the "*International Symposium on Exploring New Horizons in Chemical Sciences*", January 10–12, **2019**, Aurangabad, India (ENHCS–2019).

References

[1]Sheldon, R. A. and Dakka, J., Heterogeneous catalytic oxidations in the manufacture of fine chemicals, *Catal. Today*,**1994,** *19,* 213. https://doi.org/10.1016/0920-5861(94)80186-X

[2]Sheldon, R. A., Catalysis and pollution prevention, *Chem. Ind. (London)*, **1997,** *1*, 12.

[3]Clark, J. And Macquarrie, D., Catalysis of liquid phase organic reactions using chemically modified mesoporous inorganic solids, *Chem. Commun.*, **1998**, *8*, 853. DOI: 10.1039/A709143E

[4]Sheldon, R. A. and Downing, R. S., Heterogeneous catalytic transformations for environmentally friendly production, *Appl. Catal., A.*, **1999,** *189*,163. https://doi.org/10.1016/S0926-860X(99)00274-4

[5]Kung, H. H., *Transition metal oxides: surface chemistry and catalysis*, Elsevier, **1989**, *45.*

[6]Henrich, V. E., Cox, P. A., *The surface science of metal oxides. Cambridge University Press*, **1996**.

[7]Noguera, C., *Physics and chemistry at oxide surfaces*. Cambridge University Press, **1996**.

[8]Salem, I., Recent Studies on the Catalytic Activity of Titanium, Zirconium, and Hafnium Oxides, *Catal. Rev.*, **2003,** *45(2),* 205. https://doi.org/10.1081/CR-120015740

[9]Kalbasi, R. J., Mosaddegh, N., Suzuki-Miyaura cross-coupling reaction catalyzed by nickel nanoparticles supported on poly(N-vinyl-2-pyrrolidone)/TiO2-ZrO2 composite, *Bull. Korean Chem. Soc.*, **2011,** *32*, 2584. https://doi.org/10.5012/bkcs.2011.32.8.2584

[10]Alonso, F., Riente, P., Yus, M., Nickel Nanoparticles in Hydrogen Transfer Reactions, *Acc. Chem. Res.*, **2011,** *44*,379. DOI: 10.1021/ar1001582

[11]Yuan, F., Ni, Y., Zhang, L., Yuan, S. and Wei, J., Synthesis, properties and applications of flowerlike Ni–NiO composite microstructures, *J. Mater. Chem. A*, **2013,** *1,* 8438. DOI: 10.1039/C3TA11219E

[12]Liu, F., Sang, Y., Ma, H., Li, Z. And Gao, Z., Nickel oxide as an effective catalyst for catalytic combustion of methane, *J. Nat. Gas Sci. Eng.*, **2017,** *41*, 1. https://doi.org/10.1016/j.jngse.2017.02.025

[13]Sachdeva, H., Dwivedi, D., Bhattacharjee, R. R., Khaturia, S. and Saroj, R., NiO Nanoparticles: An Efficient Catalyst for the Multicomponent One-Pot Synthesis of Novel Spiro and Condensed Indole Derivatives, *J. Chem.*, **2012,** *2013.* http://dx.doi.org/10.1155/2013/606259

[14]Morozov, Y. G., Belousova, O. V. and Kuznetsov, M. V., Preparation of nickel nanoparticles for catalytic applications, *Inorg. Mater.*, **2011,** *47*, 36. https://doi.org/10.1134/S0020168510121027

[15]Polshettiwar, V., Baruwati, B. and Varma, R. S., Nanoparticle-supported and magnetically recoverable nickel catalyst: a robust and economic hydrogenation and transfer hydrogenation protocol, *Green Chemistry*, **2009,** *11*, 127. DOI: 10.1039/B815058C

[16]Peck, M. A., Langell, M. A., Comparison of nanoscaled and bulk NiO structural and environmental characteristics by XRD, XAFS, and XPS, *Chem. Mater.*, **2012,** *24*, 4483. DOI: 10.1021/cm300739y

[17]Imran Din, M. and Rani, A., Recent Advances in the Synthesis and Stabilization of Nickel and Nickel Oxide Nanoparticles: A Green Adeptness, *Int. J. Anal. Chem.*, **2016,** *2016.* http://dx.doi.org/10.1155/2016/3512145

[18]Jiang, Z., Xie, J., Jiang, D., Wei, X., Chen, M., Modifiers-assisted formation of nickel nanoparticles and their catalytic application to p-nitrophenol reduction, *Cryst. Eng. Comm.*, **2013,** *15*, 560. DOI: 10.1039/C2CE26398J

[19]Foo, Y. T., Chan, J. E. M., Ngoh, G. C., Abdullah, A. Z., Horri, B. A., Salamatinia, B., Synthesis and characterization of NiO and Ni nanoparticles using nanocrystalline cellulose (NCC) as a template, *Ceram. Int.*, **2017,** *43*, 16331. https://doi.org/10.1016/j.ceramint.2017.09.006

[20]Theivasanthi, T., Alagar, M., *ArXiv preprint arXiv*, Chemical Capping Synthesis of Nickel Oxide Nanoparticles and their Characterizations Studies, DOI: 10.5923/j.nn.20120205.01, **2012,** *1212*, 4595.

[21]Wang, X., Yang, Z., Sun, X., Li, X., Wang, D., Wang, P. and He, D., NiO nanocone array electrode with high capacity and rate capability for Li-ion batteries, *J. Mater. Chem.*, **2011,** *21*, 9988. DOI: 10.1039/C1JM11490E

[22]Venkat Narayan, R., Kanniah, V., and Dhathathreyan, A., Tuning size and catalytic activity of nano-clusters of cobalt oxide, *J. Chem. Sci.*, **2006,** *118(2), 179.* DOI https://doi.org/10.1007/BF02708470

Received: 03.03.2019.
Accepted: 19.03.2019.

SIMULTANEOUS EFFECTS OF Cd(II) AND Pb(II) IONS AND γ-IRRADIATION ON STABILITY OF *SPIRULINA PLATENSIS*

J. Monaselidze,[a] E. Gelagutashvili,[a] N. Bagdavadze,[a] M. Gorgoshidze[a] and E. Lomidze[a]

Keywords: metal ions; γ-irradiation; *Spirulina platensis;* differential scanning microcalorimetry.

Effect of toxic metal ions Cd(II) and Pb(II) on cyanobacterium (blue-green algae) *Spirulina platensis* intact cells have been studied with optical and differential scanning microcalorimetry (DSC) methods after 7.2 kGy ^{137}Cs gamma irradiation and without irradiation. It is shown that the addition of metal ions causes a decrease in optical absorption spectra band intensities. In the case of irradiation, the absorption band intensity decreases higher than without irradiation. The binding constant of Pb(II) with *Spirulina platensis* is calculated for nutrition medium with pH 9.2. DSC data show that Cd(II) and Pb(II) ions do not change the integral heat of absorption (ΔH_m) that equals to 24.6 J g^{-1}. In the case of irradiation, the DSC melting curve profile changes significantly and ΔH_m decreases two times, which indicates that 50 % of proteins are denaturated. The DSC method also gives a possibility to evaluate C-phycocyanin content from deconvoluted heat absorption peak at 50 °C, which equals to 35.5 %. In case of irradiated wet mass, sub-cultured wet mass, and wet mass re-irradiated with the same dose, contents of *Spirulina platensis* ingredients – C-phycocyanin, chlorophyll, and carotenoids – increase as a result of the simultaneous effect of the metal ions and irradiation.

* Corresponding Authors
E-Mail: Jamlet.monaselidze@tsu.ge; eterige@gmail.com
[a] I. Javakhishvili State University, E. Andronikashvili Institute of Physics. 6 M. Tamarashvili Str., Tbilisi, 0177, Georgia

Introduction

Nanotechnology gives a possibility to introduce a lot of new tools to be used in cellular and molecular biology. One of the modern trends in nanotechnology is associated with using the blue-green microalgae (cyanobacteria) *Spirulina platensis* that have been utilized in the food industry, pharmaceuticals, medicine and science.[1] It is one of nature's first photosynthetic organisms capable of converting light directly for complex metabolic processes. One of the algae's useful qualities is its ability to protect us from radiation. Algae contain a large amount of iodine and sodium alginate that help removal of radioactive substances from the living organisms.

It was shown[2] that *Spirulina* is a ubiquitous organism. *Spirulina platensis* has attracted more attention because of its high nutritional content that includes 50–70 % protein and minerals, vitamins, amino acids, essential fatty acids, etc.[3] The thermal stability of C-phycocyanin from *Spirulina platensis* and the compounds that additionally stabilize C-phycocyanin are crucial to food industry.[4] *Spirulina platensis* absorbs toxic metal ions from its environment.[5] It was also demonstrated that some compounds of the algal cell biomass are responsible for binding to various ions.[6,7] *Spirulina platensis* may be able to reduce many types of harmful stresses, including those caused by heavy metals and irradiation.[8,9] In our previous works, the accumulation and biosorption of metal ions by *Spirulina platensis* and their components[10–13] as well as *Spirulina platensis* usability as a matrix for production of noble metal nanoparticles[14,15] have been studied.

Thermostability of *Spirulina platensis* cells and their component have been successfully studied with the help of differential scanning microcalorimetry (DSC).[16,17]

At present, some innovative technologies are focused on the metal binding capacities of various microorganisms and their components. However, the mechanism of their interaction with metal ions and gamma irradiation are unknown. In this work, we have studied the simultaneous effects of ^{137}Cs gamma irradiation and toxic metal ions on the growth of *Spirulina platensis* intact cells and their constituents using UV–VIS spectrometry and DSC.

Materials and methods

Spirulina platensis IPPAS B–256 strain was cultivated in a standard Zarrouk[18] alkaline saline medium at 34 ºC, illumination ~5000 lux, at constant mixing in batch cultures.[19] Cultivation of the *Spirulina platensis* cells was conducted for 7 days. The cell growth was evaluated by optical density by monitoring of changes in absorbance at wavelength 560 nm measured with a spectrophotometer (UV–Visible spectrometer, Cintra 10e GBC Scientific Equipment Pty Ltd, Australia). The absorption spectra from 380 to 850 nm of intact cells suspension of *Spirulina platensis* (pH 9.2) in Zarrouk medium have been recorded. In all abovementioned cases, the concentration of *Spirulina platensis* was 1.6 mg mL^{-1}. This was determined by instrumental measurements.[20,21] The concentration of Cd(II) and Pb(II) ions was 0.5 μM.

To study the biosorption process on the *Spirulina platensis* intact cells, the methods of dialysis and atomic absorption analysis were used. A known quantity of cyanobacterium suspension in the nutrient medium was in contact with the solution containing a known concentration of metal ions.

The intact cell weight content was kept constant (1.6 mg mL^{-1}), while the initial metal concentration varied within the interval 10^{-3} to 10^{-6} M. All experiments were carried out at the ambient temperature. The dialysis was carried out in 5 mL cylindrical vessels made of organic glass. A 30μm wide cellophane membrane (Visking type, manufactures by Serva) was used as a partition. The duration of dialysis was 72 h. The metal concentration after the dialysis was measured using the atomic absorption spectrophotometer Analyst–900 (Perkin-Elmer). Each value was determined as an average of three independent estimated values with the standard deviation.

Spirulina platensis cells were exposed to 7.2 kGy γ-irradiation using ^{137}Cs as a γ-source, at the Applied Research Center, E. Andronikashvili Institute of Physics. After the irradiation, the cells were cultivated in Zarrouk medium for 21 days. The adsorption isotherm data for metal ion binding by *Spirulina* cells were calculated from the Freundlich equation.[22]

The *Spirulina platensis* cell suspension and wet mass were also measured with DSC designed for diluted solutions and complex biological systems.[23] The calorimeter sensitivity was 0.1 μW, the volume of measuring vessels was 0.3 cm^3, the heating rate was 0.5 °C min^{-1}, and the temperature range of measurements was from 25 to 130 °C. The accuracy of the temperature measurements was not less than 0.05 °C. The error in the determination of melting enthalpy (ΔH_m), heat capacity dQ/dT (ΔC_{max}) was not more than 10 %.

Results and discussions

Cd(II) and Pb(II) ions effect on intact cells of *Spirulina platensis* was studied as a function of metal concentration at pH 9.2. The spectrum of native S. platensis biomass is illustrated in Fig. 1. Figure 1 shows the absorption characteristics of control of intact cells of *Spirulina platensis*. The peak at 681 nm corresponds to the absorption of chlorophyll *a* (Chl *a)*. The peaks at 620.7 nm and 500 nm correspond to the absorption of phycocyanin and carotenoids, respectively. A peak at 440 nm corresponds to Soret band of Chl *a*.[24] In Fig. 1, there are also shown the effects of Pb(II) and Cd(II) ions on the absorption of the intact cells of *Spirulina platensis*.

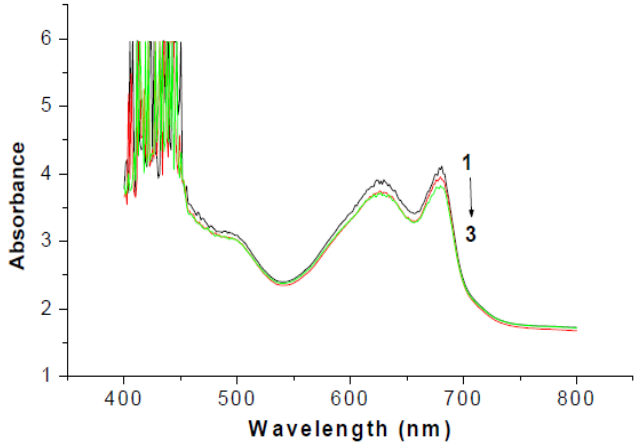

Figure 1. Absorption spectra of intact cells of cyanobacterium *Spirulina platensis*. 1 – control after incubation in nutrition medium for 7 d, 2 – same control + Pb(II), and 3 – same control + Cd(II).

Figure 1 demonstrates that the absorption intensity decreases after addition of the metal ions. The absorption is inhibited by 8, 3, 3 and promoted by 33 % at 681, 620.7, 500 and 440 nm, respectively, for Cd(II) comparing to the control. Similar results were obtained for Pb(II) – the absorption intensity was inhibited by 5, 3 and 3 % and increased by 33 % at the given wavelengths, respectively.

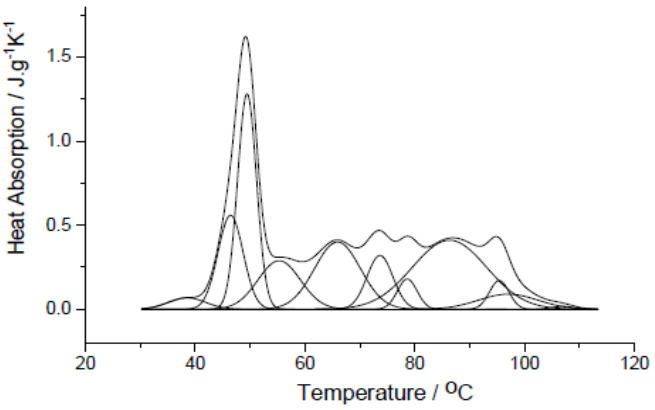

Figure 2. Heat absorption curve of intact *Spirulina platensis* cells recalculated per gram of biomass in Zarrouk medium. Conditions are the same as in Fig.1. The volume of cell suspension was 290 μl and dry biomass amount was 3.5 mg.

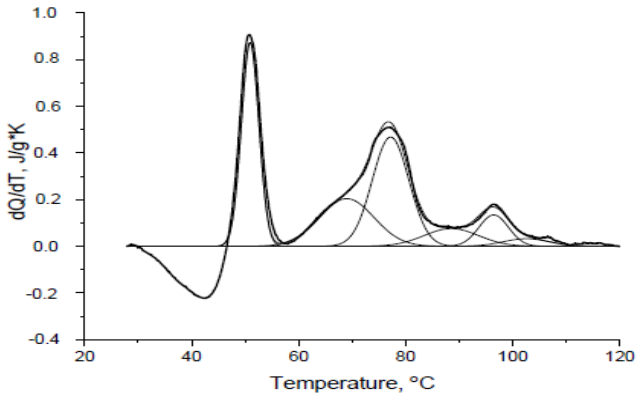

Figure 3. Heat absorption curve of intact *Spirulina platensis* cells in the presence of 0.5 μM Cd(II) recalculated per gram of biomass in Zarrouk medium. Conditions are the same as in Figure 1. The volume of cell suspension was 290 μl and dry biomass amount was 3.7 mg.

Figures 2–4 present heat absorption curves of *Spirulina platensis* intact cells suspensions and cells treated with Cd(II) and Pb(II) ions. The given data demonstrate that *Spirulina platensis* cell components and intercellular matrix proteins, including genetic material, melt within the temperature range from 45 to 110 °C. The intact samples and samples with metal ions have some similarities and differences. They are similarities in appearance of an intensive endothermic maximum at 50 °C in case of intact cells and curves of cells treated with Cd(II) and Pb(II) ions. The differences appear in melting characteristic in the temperature range from 58 to 100 °C. For example, the melting curves of intact cells are complicated - includes heat absorption peaks at 65, 74, 78, 86, and 95 °C and a shoulder at around 58 °C – while the curves for metal-ion treated cells are simpler.

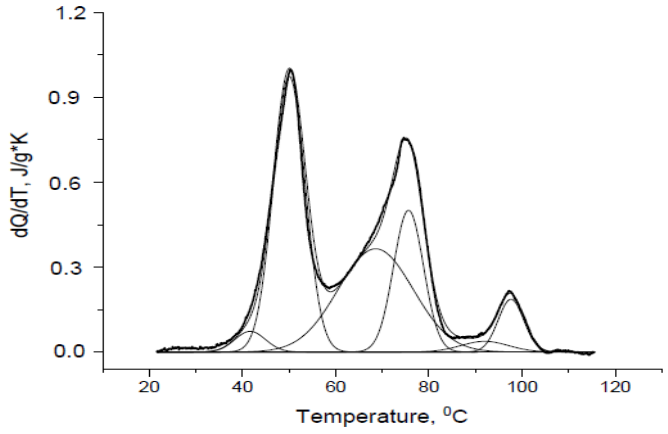

Figure 4. Heat absorption curve of intact *Spirulina platensis* cells in the presence of 0.5 µM Pb(II) recalculated per gram of biomass in Zarrouk medium. Conditions are the same as in Figure 1. The volume of cell suspension was 290 µl and dry biomass amount was 4.2 mg.

The curve profile changes to simpler curves in case of metal-ion treated samples contains only two separated peaks at 78 and 98 °C. As for the very weak absorption peak of chromatin at 105 °C, its thermostability does not change at the mentioned content of metal ions.[23] The melting enthalpy of intact *Spirulina platensis* and *Spirulina platensis* at the presence of 0.5 µM Cd(II) and Pb(II) ions coincide within the experimental error and equals to 24.6 J g^{-1}.

Figures 3 and 4 demonstrate that Cd(II) or Pb(II) ion concentration 0.5 µM do not damage the genetic material, but those ions change the melting curve profile, which is caused by the formation of two independent heat absorption peaks at around 78 and 97 °C. The curve deconvolution shows that the protein melting at 78 and 97 °C takes place in narrow temperature intervals, which indicate that the proteins influenced by Cd(II) and Pb(II) have high thermostability and they have highly ordered structures. It should be mentioned that we have observed a powerful heat evolution (–*Q*) in case of cells at presence of Cd(II) in the temperature range 30 to 50 °C, which mainly reflects respiration of cells (oxygen absorption rate), which in its turn, strongly depends on pH and heating rate.[17] As far as the primary goal of this work is focused on influence of Cd(II) and Pb(II) ions on thermodynamic stability of proteomes and protein complex of *Spirulina platensis* that is denaturated in the temperature interval from 45 to 110 °C, we kept the samples in dark at 15 °C during 30 h in sealed DSC cells before experiments, in order to have –*Q* equal to about 0 J g^{-1}. This was made to have a proper baseline for precise detection of melting parameters.

Figure 5 illustrates the absorption spectra of the intact cells of the *Spirulina platensis* as a control, (1) after 7.2 kGy γ-irradiation for 7 days, (2) control after 7.2 kGy γ-irradiation in the presence of Pb(II) ions, and (3) control after 7.2 kGy γ-irradiation in the presence of Cd(II) ions. After irradiation, the peak intensities were decreased as follows: by 20, 11, 22 and 28 % at 681, 620.7, 500 and 440 nm, respectively, for Cd(II) ions in comparison to the irradiated control. As for Pb(II), the peak intensities were decreased by 14, 7, 18 and 20 % at the given wavelengths, respectively.

As it is seen from the abovementioned results, in both cases, cadmium(II) ions have a more significant effect on peak intensities than the lead(II) and the optical spectra positions do not change due to the effect of metals.

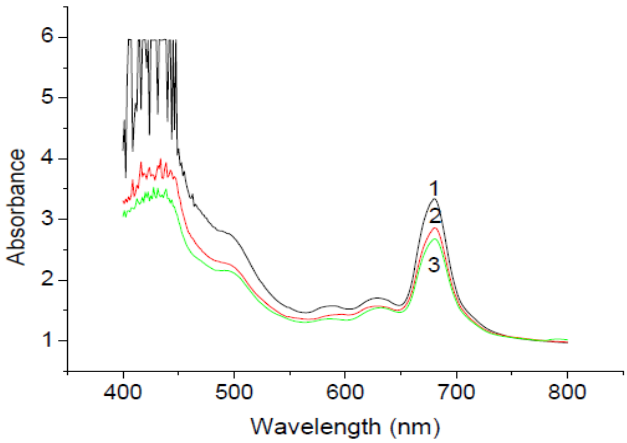

Figure 5. Absorption spectra of intact cells of the cyanobacterium, *Spirulina platensis*. 1 – control after incubation 7 days, 2 – control after γ-irradiation with 7.2 kGy dose + Pb(II), and 3 – control after γ-irradiation with 7.2 kGy dose + Cd(II).

The equilibrium constant was determined by the use of equilibrium dialysis and atomic absorption analysis methods for Pb(II) ions. Figure 6 presents the absorption isotherm for Pb(II) – *Spirulina platensis* in nutrient medium at pH 9.2, where the Freundlich adsorption model was used for the mathematical description of the biosorption of Pb(II) – *Spirulina platensis.* The points presented in the figure are experimental data, and the line is derived from the Freundlich equation. The correlations between experimental data and the theoretical equation were extremely good with R^2 above 0.90. Using the Freundlich isotherm, the biosorption constant (*K*) was determined for Pb(II)–*Spirulina platensis* system and were found to be equal as $1.8 \cdot 10^{-4}$ M.

The Cd(II)–*Spirulina platensis* system sorption constant value exceeds the value given for Pb(II)–*Spirulina platensis* system in the nutrient medium.[10,11] The biosorption constant for Cd(II) – *Spirulina platensis* was dissolved in the medium at pH 8.6 was $5.1 \cdot 10^{-4}$ M. We foundus that the efficiency of Cd(II) ions biosorption depends on the conditions of the uptaking processes,[10,11] especially, the pH is an essential factor for Cd(II) binding of *Spirulina platensis*.

It was supposed[25] that Cd(II), Cu(II), and Co(II) biosorption by algae biomass takes place through electrostatic interactions between the metal ions and the microbial cell walls. The results showed that carboxyl groups on algal cell biomass are the active sites for binding to various ions.[26]

Figure 7 demonstrates irradiation of wet mass (control) that was sub-cultured after 7.2 kGy gamma irradiation for 3 weeks, as well as the influence of Cd(II) and Pb(II) ions (Curves 2 and 3). Figure 7 shows that the absorption intensity decreases in addition of either metal ion.

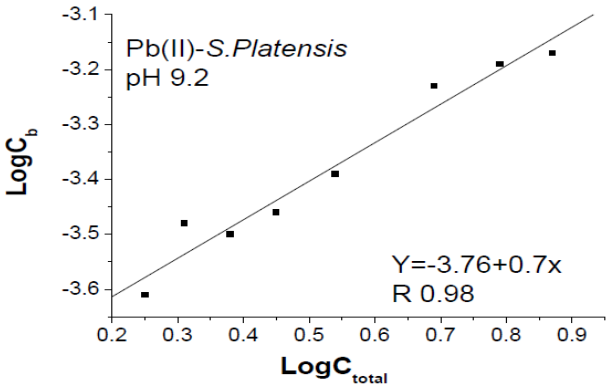

Figure 6. Linearized Freundlich adsorption isotherms of Pb(II)–*Spirulina platensis* in nutrition medium (C_b is binding metal concentration, mg g^{-1}, and C_{total} is initial Pb concentration. mg L^{-1}).

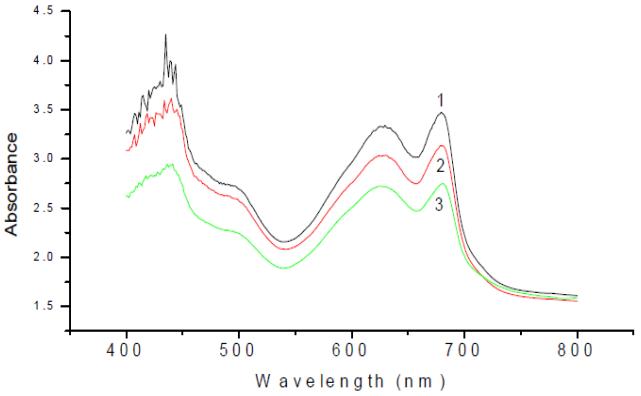

Figure 7. Absorption spectra of intact cells of cyanobacterium *Spirulina platensis*. 1 – control that was sub-cultured after 7.2 kGy γ-irradiation for 3 weeks, 2 – control that was sub-cultured after 7.2 kGy γ-irradiation for 3 weeks + Pb(II), and 3 – control that was sub-cultured after 7.2 kGy γ-irradiation for 3 weeks + Cd(II)

Namely, the absorption intensity decreased by 21 % at 681 nm, by 16 % at 620.7 nm, by 17 % at 500 nm, and by 25 % at 440 nm for Cd(II) ions, in comparison to the control.

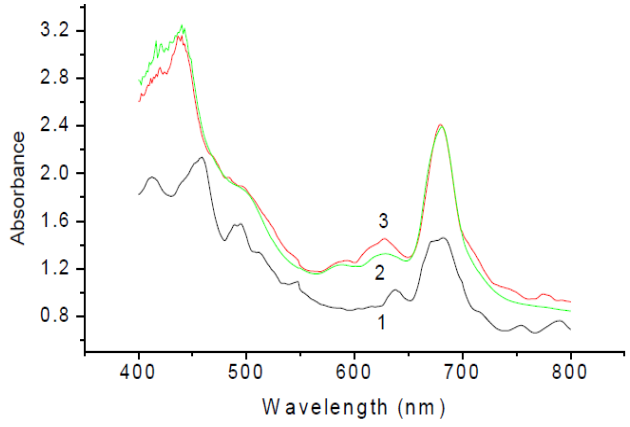

Figure 8. Absorption spectra of intact cells of cyanobacterium *Spirulina platensis*. 1 – irradiated mass that was sub-cultured after 7.2 kGy γ-irradiation for 3 weeks after repeated irradiation with same dose, 2 – irradiated mass that was sub-cultured after 7.2 kGy γ-irradiation for 3 weeks after repeated irradiation with same dose + Cd(II), and 3 – irradiated mass that was sub-cultured after 7.2 kGy γ-irradiation for 3 weeks after repeated irradiation with same dose + Pb(II).

As for Pb(II), the absorption intensity decreased by 10, 6, 4 and 8 % at the given wavelengths, respectively, in comparison to the irradiated wet mass.

Figure 8 demonstrates the absorption spectra of the intact cells of the irradiated *Spirulina platensis* mass that was sub-cultured for 3 weeks after 7.2 kGy γ-irradiation, and after repeated irradiation with the same dose and under effects of Cd(II) and Pb(II) ions. Curve 2 corresponds to Cd(II), and Curve 3 corresponds to Pb(II). At the presence of Cd(II) ions, the absorption intensity increased by 64, 49, 26 and 69 % at 681, 620.7, 500 and 440 nm, respectively, in comparison to the irradiated wet mass. At the presence of Pb(II), the absorption intensities are increased by 64, 59, 27 and 64 %, respectively, at the same wavelengths. Thus, the toxic metal ions promote an increase in the amount of basic components of *Spirulina platensis*. Namely, the presented study has demonstrated that proteins, chlorophylls and carotenoids content of *Spirulina platensis* significantly increases in comparison to the control as a result of the simultaneous effect of Cd(II) and Pb(II) ions and γ-irradiation.

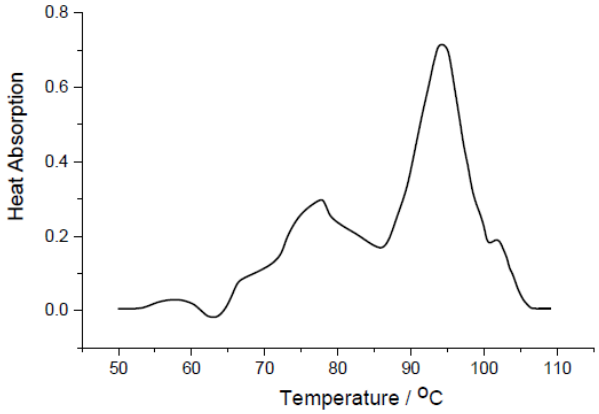

Figure 9. Differential scanning microcalorimetry curve of irradiated native *Spirulina platensis* cells. Conditions are the same as in Figure 8. The volume of cell suspension was 290 µl and dry biomass amount was 2.1 mg.

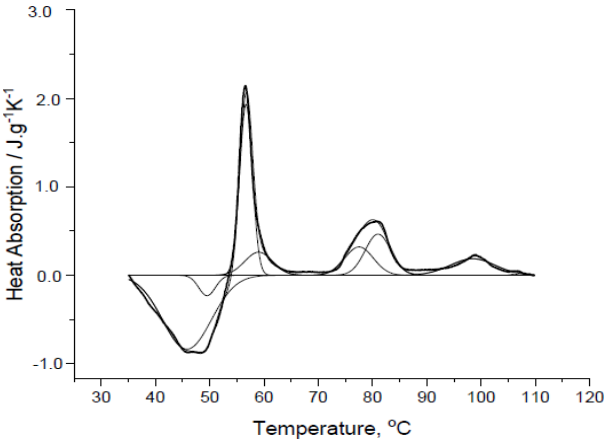

Figure 10. Heat absorption curve of irradiated and recultivated *Spirulina platensis* cells recalculated per gram of biomass in Zarrouk medium. Conditions are the same as in Figure 7. The volume of cell suspension was 290 µl and dry biomass quantity was 4.05 mg.

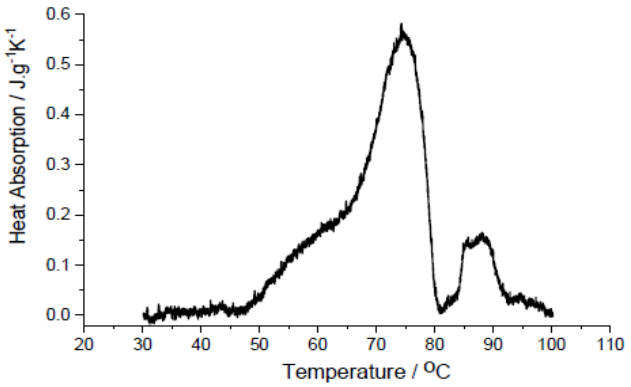

Figure 11. Heat absorption curve of re-irradiated *Spirulina platensis* cells recalculated per gram of biomass in Zarrouk medium. Conditions are the same as in Figure 8. The volume of cell suspension was 290 µl and dry biomass amount was 1.2 mg.

The DSC measurements show that the irradiated *Spirulina platensis* cell suspension has a complex melting profile with weak maximums at 72 and 92 °C and a shoulder at 103 °C, the C-phycocyanin melting peak at 50 °C has been disappeared, and proteins mainly melt at 72 and 92 °C (Figure 9). We suppose that the shoulder corresponds to melting of genetic material – chromatin complex.[23] The integrated heat amount is decreased to the half comparing to the non-treated sample (see Figure 2). After 3 weeks of recultivation, the same *Spirulina platensis* cell suspension has the curve presented in Figure 10, where the C-phycocyanin heat absorption intensity is restored and the melting temperature is shifted to higher temperatures by 6 °C, and the peak around 105 °C is very weak. For comparison, see also Figure 11.

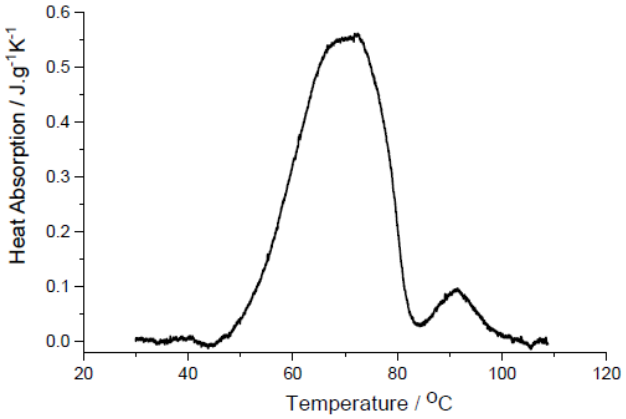

Figure 12. Heat absorption curve as a function of the temperature of re-irradiated *Spirulina platensis* cells at the presence of 0.5 µM Pb(II) recalculated per gram of biomass in Zarrouk medium. Conditions are the same as in Figure 8. The volume of cell suspension was 290 µl and dry biomass quantity was 1.3 mg.

Figure 12 presents the DSC curve of re-irradiated *Spirulina platensis* cells at the presence of 0.5µM Pb(II). The curve shows that the C-phycocyanin peak absent, the main heat absorption occurs as a broad dominant peak around 72 °C, and a small peak appears at about 93 °C. The melting enthalpy is decreased to 1/3 compared to the intact cells. Similar results have been received for Cd(II.

The DSC data can give the value of absorption heat with high accuracy in the denaturation/melting process of *Spirulina platensis* cells, therefore these peaks could be deconvoluted. Since the C-phycocyanin melts in the temperature range from 40 to 58°C (T_m = 50±1°C), from the heat calculated from the area under this peak, the C-phycocyanin content is proved to be 35±5 % of total protein amount that melts in the temperature range from 40 to 100 °C in case of *Spirulina platensis* in Zarrouk medium.

Acknowledgment

Paper was presented at the 5th International Conference "Nanotechnologies", November 19–22, 2018, Tbilisi, Georgia (Nano–2018).

References

[1]Vonshak, A., *Spirulina platensis* (Arthrospira): *Physiology, Cell Biology and Biotechnology* (1st Ed.), **1997**, London, Taylor and Francis Ltd.

[2]Orio, C., *Spirulina*, the edible microorganism, *Microbiol. Rev*., **1983**, *47*, 551.

[3]Campanella, L., Crescentini, G., Avino, P., Chemical composition and nutritional evaluation of some natural and commercial food products based on Spirulina, *Analusis*, **1999**, *27*, 533. https://doi.org/10.1051/analusis:1999130

[4]Martelli, G., Folli, C., Visaic, L., Daglia, M., Ferrari. D., Thermal stability improvement of blue colorant C-Phycocyanin from Spirulina platensis for food industry applications, *Process Biochem*., **2014**, *49(1)*, 154.

https://doi.org/10.1016/j.procbio.2013.10.008

[5]Slotton, D. G., Goldman, C. R., Frank. A., Commercially grown spirulina found to contain low levels of mercury and lead, *Nutr. Rep. Int*., **1989**, *40(2)*, 1165.

[6]Gardea–Torresdey, J. L., Becker–Hapak, M. K., Hosea, J. M., Darnell. D. W., Effect of chemical modification of algal carboxyl groups on metal ion binding, *Environ. Sci. Technol*., **1990**, *19*, 1372. https://doi.org/10.1021/es00079a011

[7]Volesky, B., Holan. Z. R., Biosorption of heavy metals, *Biotechnol. Prog*., **1995**, *11*, 235. https://doi.org/10.1021/bp00033a001

[8]Sharma, K. K., Schuhmann, H., Schenk, P. M., High Lipid Induction in Microalgae for Biodiesel Production, *Energies*, 2012, 5, 1532.https://doi.org/10.3390/en5051532

[9]Cheng, J., Huang, Y., Feng, J., Sun, J., Zhou, J., Cen, K., Mutate Chlorella sp. by nuclear irradiation to fix high concentrations of CO_2, *Bioresource Technol*., **2013**, *136*, 496. https://doi.org/10.1016/j.biortech.2013.03.072

[10]Gelagutashvili, E., "Ch. 9. *Biosorption of heavy metals by Spirulina Platensis and their Components*," in Plants and Microbes, P. Goyal, A. Chauhan, and P. Kaushik, Eds., Mumbai, **2014**, 154–174.

[11]Gelagutashvili, E., Comparative Study on Heavy Metals Biosorption by Different Types of Bacteria, *Open J. Metal*, **2013**, *3*, 62.https://doi.org/10.4236/ojmetal.2013.32a1008

[12]Gelagutashvili, E., Tsakadze, K., Effect of Hg(II) and Pb(II) Ions on C-Phycocyanin (*Spirulina platensis*) , *Optics Photonics J*., **2013**, *3*, 122. https://doi.org/10.4236/opj.2013.31020

[13]Gelagutashvili, E., Cyanobacteria *Spirulina Platensis* Basic Protein C-Phycocyanin and Zn(II) Ions, *Am. J. Nano Res. Appl.*, **2017**, *5(3-1)*, 5**.** doi: 10.11648/j.nano.s.2017050301.12

[14]Kalabegishvili, T. L., Murusidze, I. G., Kirkesali, E. I., Rcheulishvili, A. N., Ginturi, E. N., Gelagutashvili, E. S., Kuchava, N. E., Bagdavadze, N. V., Janjalia, M. V., Pataraya, D. T., Gurielidze, M. A., Frontasyeva, M. V., Zinicovscaia, I. I., Pavlov, S. S., Tsertsvadze, G. I., Gabunia, V. N., *Eur. Chem. Bull., 2015, 4(1),* 43. DOI: http://dx.doi.org/10.17628/ecb.2015.4.43-49

[15]Kalabegishvili, T., Murusidze, I., Kirkesali, E., Rcheulishvili, A., Ginturi, E., Kuchava, N., Bagdavadze, N., Gelagutashvili, E., Frontasyeva, M. V., Zinicovscaia, I., Pavlov, S. S., Dmitriev, A. Y., Gold and silver nanoparticles in Spirulina platensis biomass for medical application, *Ecol. Chem. Eng. S*, **2013**, *20(4)*, 621. https://doi.org/10.2478/eces-2013-0043

[16]Topchishvili, L., Barbakadze, Sh., Khizanishvili, A., Majagaladze, G., Monaselidze, J., Microcalorimetric Study of Iodized and Noniodized Cells and C-Phycocyanin of *Spirulina platensis*, *Biomacromolecules*, **2002**, *3(3)*, 415.

[17]Monaselidze, J., Barbakadze, Sh., Kvirikashvili, Sh., Majagaladze, G., Khachidze, D., Topchishvili, L., Thermal Characteristics ofSpirulina platensisCells under Nongrowing Conditions at Various Values of pH Medium, *Biomacromolecules*, **2002**, *3(4)*, 783.

[18]Zarrouk, C., Contribution al'etuded'unecyanophycee. Influence de Divers Facteurs Physiques Etchimiquessurlacroissance et Photosynthese de Spirulina maxima, PhD Thesis, **1966**, Paris, University of Paris.

[19]Mosulishvili, L., Belokobilsky, A., Gelagutashvili, E., Rcheulishvili, A., Tsibakhashvili. N., The study of the mechanism of cadmium accumulation during the cultivation of *Spirulina platensis*, *Proc. Georg. Acad. Sci. (Ser. Biol.)*, **1997**, *23(1-6)*, 105.

[20]Bennet, A., Bogorad, L., Complementary chromatic adaptation in a filamentous blue-green alga, *J. Cell Biol*., **1973**, *58*, 419. https://doi.org/10.1083/jcb.58.2.419

[21]Patel, A., Mishra, S. M., Pawar, R., Ghosh, P., Purification and characterization of C-Phycocyanin from cyanobacterial species of marine and freshwater habitat, *Protein Express. Purif*., **2005**, *40*, 248. https://doi.org/10.1016/j.pep.2004.10.028

[22]Freundlich. H., Over the adsorption in solution**,** *Z. Phys. Chem.*, **1906**, *57*, 384.

[23]Monaselidze, J., Abuladze, M., Asatiani, N., Kiziria, E., Barbakadze, Sh., Majagaladze, G., Iobadze, M., Tabatadze, L., Holman, H.-Y., Sapojnikova, N., Characterization of chromium-induced apoptosis in cultured mammalian cells, *Thermochim. Acta*, **2006**, *441*, 8. https://doi.org/10.1016/j.tca.2005.11.025

[24]Fork, D. C., Mohanty, P., In: *Light Emission by Plants and Bacteria* (Eds. A. J. Govindjee, D. C. Fork), **1986**, New York, Academic Press, 451.

[25]Kuyucak, N., Voleskym, B., Biosorbents for recovery of metals from industrial solutions, *Biotechnol. Lett.*, **1988**, *10(2)*, 137. https://doi.org/10.1007/bf01024641

[26]Plaza, M., Cifuentes, E., Ibanez, A., In the search of new functional food ingredients from algae, *Trends Food Sci. Technol*., **2008**, *19*, 31.

https://doi.org/10.1016/j.tifs.2007.07.012

[27]Privalov, P. L., In: *Microcalorimetry of Macromolecules*: *The Physical Basis of Biological Structures*, **2012**, Hoboken, Wiley, 225.

Received: 06.01.2019.
Accepted: 20.03.2019.

KINETICS OF ISOTHERMAL ANNEALING OF γ-IRRADIATED EUTECTIC MIXTURE OF $NaNO_3$-KNO_3

Pawar S. S.[a] and Patil S. F.[b]

Keywords: annealing; kinetics; γ-irradiation; eutectic of $NaNO_3$-KNO_3.

A considerable amount of work has been reported on isothermal annealing of pure alkali and alkaline earth metal nitrates. In the present work, initially, the eutectic of $NaNO_3$-KNO_3 was prepared by mixing $NaNO_3$ (45%) and KNO_3 (55%) fused at 225 ^{0}C and cooled naturally. The samples of a eutectic of $NaNO_3$-KNO_3 were irradiated in ^{60}Co – gamma source. The radiation decomposition of the eutectic mixture takes place. Present work mainly deals with the study of isothermal annealing of radiation damage in a eutectic mixture of $NaNO_3$-KNO_3. This data has been analyzed by using conventional kinetics and the Waite model. Results of annealing show that a significant fraction of annealing obeys second order kinetics except in the initial short period. The energies of activation are calculated by two methods and are found to agree.

* Pawar S. S.
E-Mail: sspawar2005@gmail.com
[a] Department of Chemistry, Fergusson College (Autonomous), Pune-411004, Maharashtra, India.
[b] Ex-Professor, Department of Chemistry, Savitribai Phule Pune University, Pune 411007, Maharashtra, India.

INTRODUCTION

A considerable amount of research results has been reported on isothermal annealing of pure alkali and alkaline earth metal nitrates,[1-7] however, only limited data are available on the annealing of eutectics.

It is well established that defect concentration in solids increases after irradiation as compared to the thermal equilibrium level. These defects are responsible for different property changes in solids. These defects react to reduce the free energy of the system. When the temperature of irradiated solids is raised sufficiently, the property reverts to its original value. This general process of decay of property-change by temperature is known as annealing.

Several workers carried out the experiments on the thermal annealing process in alkali and alkaline earth nitrates.[8-10]. The kinetic analysis showed that the order of reaction varied concerning the nature of nitrates. Bedekar et. al[2] reported 100 % annealing of damage in ammonium nitrate crystals and about 35 % annealing to take place in KNO_3-$Sr(NO_3)_2$ eutectic at 200 ^{0}C.

The process of annealing is generally formulated using equations similar to those of chemical kinetics. Various diffusion-controlled models have been proposed such as Fletcher-Brown model and Waite model[11,12] to explain the characteristics of annealing kinetics. The energy of activation for the annealing reaction is computed. An appropriate mechanism of annealing consistent with the observed results is proposed.

EXPERIMENTAL

The eutectic mixture of $NaNO_3$ (45 %)-KNO_3(55 %) was fused at 225^0 C and cooled naturally.[13] The irradiation of samples of eutectic was carried out in 2.5 kCi ^{60}Co γ-source at ambient temperature. The results of the radiolytic decomposition of a eutectic mixture of $NaNO_3$-KNO_3 are already reported in terms of $G(NO_2^-)$ values.

After irradiation, the samples of the eutectic mixture of $NaNO_3$-KNO_3 were subjected to isothermal annealing at various temperatures for different time intervals using an electric furnace.

The annealed samples of the eutectic mixture after removal from thermostat or furnace were analyzed to estimate the amount of nitrite [$G(NO_2^-)$] left after annealing by using Shinn's method.[14]

RESULTS AND DISCUSSION

The fraction annealed, ø, after heating for time *t*, is defined by an expression

$$ø = (NO_2^-)_0 - (NO_2^-)_t/(NO_2^-)_0$$

where, $(NO_2^-)_0$ and $(NO_2^-)_t$ are the concentrations expressed in a number of NO_2^- molecules per gram of the eutectic mixture present initially and after time *t*, respectively.

A plot of fraction annealed ø, as a function of annealing time at various temperatures, are shown in Fig. 1. The examination of the annealing curves obtained reveals that there is an abrupt recovery of damage in the initial period of annealing followed by a slow rate of annealing at every temperature.

For example, the extent of annealing in a eutectic mixture of $NaNO_3$-KNO_3 at 200 ^{0}C is found to be 45 % in 10 h, while only 10 % of annealing takes place during the next 20 h.

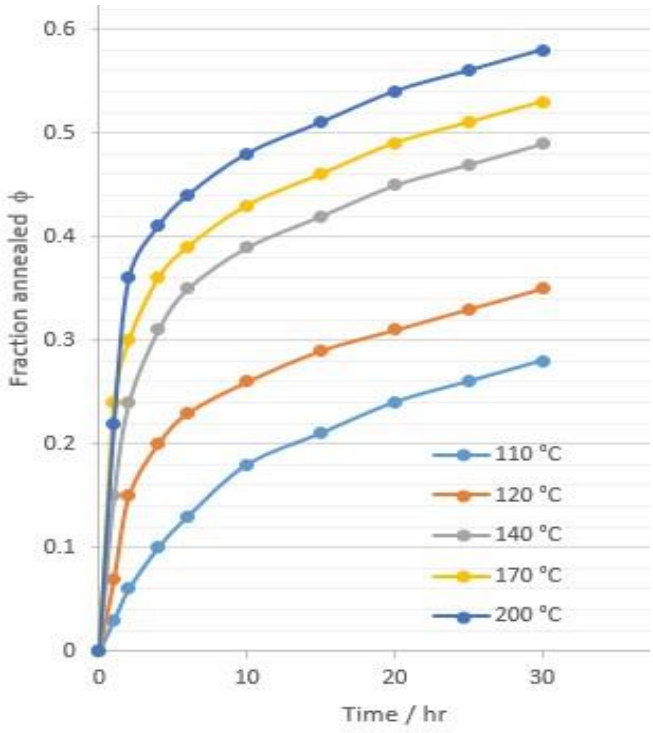

Figure 1. A plot of fraction annealed ø, as a function of annealing time at various temperatures

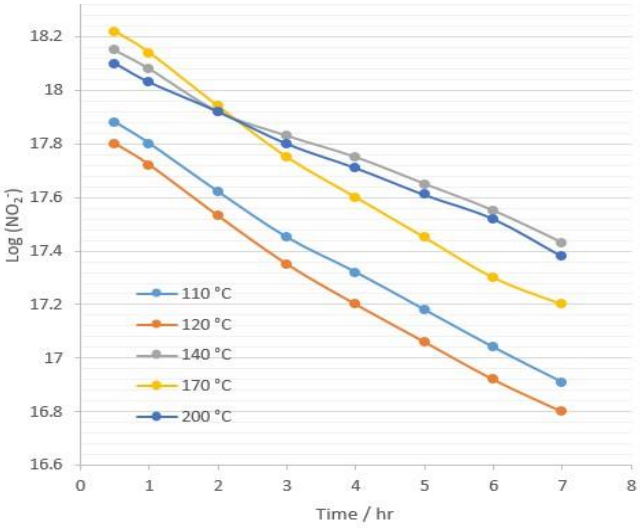

Figure 2. First order plots for annealing of nitrite in γ–irradiated $NaNO_3$-KNO_3 eutectic.

Analysis of data of annealing obtained at various temperatures by conventional kinetics[5] showed that the annealing occurs by a combination of the first and the second order processes. The first order process taking place in the initial stages is attributed to the germinate recombination of fragments in the damaged zone. The first order disappearance of the nitrite is the recovery of closely correlated NO_2^- and O pairs in the form of NO_3^- (Fig. 2).

While, the occurrence of the second order is explained on the basis of a random combination of NO_2^- and O or O_2 fragments which have diffused farther apart in the crystal lattice. (Fig. 3)

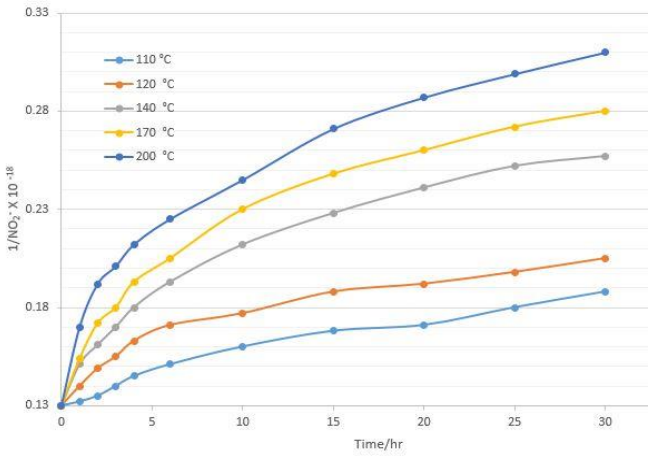

Figure 3. Second order plots for annealing of nitrite in γ–irradiated $NaNO_3$-KNO_3 eutectic.

The energy of activation for the first and the second order processes computed from the Arrhenius plot are found to be 8.0 kJ. mol^{-1} and 14.4 kJ mol^{-1} respectively. The kinetics of annealing is also explored by using the Waite Model which considers the annealing as a diffusion-controlled reaction. This model envisages a spread in the separation of an interstitial from the corresponding vacancy and a random distribution of pairs concerning one another. The resulting expression for short time of annealing is

$$ø = K \{D_0 e^{-E/RT}\}^{1/2} t^{1/2}$$

where,

D_0 is the diffusion coefficient and

E is the energy of activation for diffusion.

The energy of activation of annealing from this is found to be 13.7 kJ mol^{-1} which is in reasonable agreement with the value obtained for the second order process using the conventional method.

CONCLUSIONS

The present investigations revealed that the recovery of damage in irradiated samples of the eutectic mixture of $NaNO_3$-KNO_3 occurs due to thermal reactions as well as reactions accompanying phase transformations in the damaged crystals.

The isothermal annealing process is formed to consist of a fast first-order reaction in addition to a slow predominant second order reaction.

Acknowledgments

The authors express their thanks to the Principal, Fergusson College (Autonomous), Pune-411004, Maharashtra, India and HOD, Department of Chemistry, Savitribai Phule Pune University, Pune 411007, Maharashtra, India.

REFERENCES

[1]Patil, S. F., Nalawade, C. G., Kinetics of the isothermal annealing of radiation damage in barium nitrate crystals, *J. Radiochem. Radioanal. Lett.*, **1980**, *45*(2), 133.

[2]Patil, S. F., Bedekar, A. G., Effect of particle size of nitrate and oxides as a heterophase impurity on the radiation decomposition of pure and Ba^{2+} doped KNO_3 crystals, *Int. J. Radiation Phys. Chem.*, **1987**, *29(2),* 121. https://doi.org/10.1016/1359-0197(87)90045-2

[3]Mahapatra, B. M., Bhatia, D., Chemical recovery of damage fragments in gamma-irradiated doped potassium nitrate, *Radiat. Phys. Chem*., **1986**, *29(5),* 339. https://doi.org/10.1016/1359-0197(86)90076-7

[4]Arnikar, H. J., Patil, B. T., Patil, S. F., Kinetics of the annealing of radiation damage in barium chlorate monohydrate *J. Radiochem. Radioanal. Lett.*, **1976,** *24(2),* 67.

[5]Samuel, J., Culas, S., Kinetics of Isothermal Annealing of Gamma-irradiation Damage in Thallous Nitrate, *Orient. J. Chem.*, **2013** *29(4).*

http://dx.doi.org/10.13005/ojc/290433

[6]Agarwal, N., Garg, A. N., Effect of cation size on the 60Co-gamma radiolytic decomposition of alkali and alkaline earth metal nitrates, *Radiat. Phys. Chem*., **2005**, *73* 147. https://doi.org/10.1016/j.radphyschem.2004.07.010

[7]Rathore N., Krishan, B., Synthesis and Characterization of Complexes of Glipizide with Zirconium and Cobalt, *Orient. J. Chem.*, **2013**, *29(3),* 1001. DOI: http://dx.doi.org/10.13005/ojc/290320

[8]Maddock, A. G., Mohanty, S. R., Thermal Annealing of Chemical Radiation Damage, *Nature*, **1959**, *182*, 1797. https://doi.org/10.1038/1821797a0

[9]Dalai, P. C., Mohanty, S. R., Kinetics of Thermal Annealing of Chemical Radiation Damage in Hexammino-Cobaltic Nitrate, *Radiochim, Acta*, 1976, *23*, 171. **DOI:** https://doi.org/10.1524/ract.1976.23.34.171

[10]Nair, S. M. K., Krishnan, M. S., James, C., Thermal decomposition of irradiated strontium nitrate, *J. Indian Chem. Soc*., **1982**, *59(10),* 1147.

[11]Waite, T. R., Theoretical Treatment of the Kinetics of Diffusion-Limited Reactions, *Phys. Rev*., **1957**, *107*, 463. DOI:https://doi.org/10.1103/PhysRev.107.463

[12]Fletcher, R. C., Brown, W. L., Annealing of Bombardment Damage in a Diamond-Type Lattice: Theoretical, *Phys. Rev*., **1953**, *92*, 585.

DOI:https://doi.org/10.1103/PhysRev.92.585

[13]Pawar, S. S., Patil, S. F., Effect of Heterophase Additives on the gamma-Radiolysis of some nitrates, eutectic mixture and Sr^{2+}-doped eutectic mixture of $NaNO_3$-KNO_3, *Int. J. Manag. Technol., Eng.*, **2018**, *8*(11), 1661.

[14]Shinn, M. B., Colorimetric method for determination of nitrite, *Ind. Eng. Chem. Anal. Ed*. **1941**, *13*, 33.

This paper was presented at the "*International Symposium on Exploring New Horizons in Chemical Sciences*", January 10–12, 2019, Aurangabad, India (ENHCS–2019).

Received: 03.03.2019.
Accepted: 20.03.2019.

PHYTOCHEMICAL PROPERTIES OF CONVENTIONAL AQUEOUS EXTRACT AND MICROWAVE ASSISTED EXTRACT OF *CESTRUM NECTURM* LEAVES

Samreen Fatema,[a] Mohd Imran Anees,[b] Mazahar Farooqui[c] and Pathan Mohd Arif[a]*

Keywords: extraction; phytochemical analysis; antibacterial activity; *Cestrum necturm*

Cestrum nocturnum Linn. belongs to Solanaceae. It is commonly known as Raat rani, lady of night or night Jessamine have great medicinal value. The plant was extracted using conventional extraction as well as microwave-assisted extraction. The phytochemicals such as carbohydrate, proteins, amino acid, glycoside, phenolic compounds and tannins have been qualitatively determined. The physicochemical properties such as relative density, viscosity, surface tension and refractive index were determined. All features of microwave assisted extract were found to be higher than aqueous extract. UV-Vis and IR data were evaluated. The extracts were screened for biological activity and aqueous extract is found to be active against *E. Coli, B. Subtilis, S. Typhi, S. Aureus, tuberculosis and malaria*

* Corresponding Authors
Tel: 09423456007
E-Mail: arif7172@rediffmail.com
[a] Postgraduate and research center, Maulana Azad College, Aurangabad (MS), India 431001
[b] Y.B Chavan College of Pharmacy, Aurangabad (MS) India 431001
[c] Dr. Rafiq Zakaria College for women, Navkhanda, Aurangabad (MS) India 431001

Introduction

Plants are the vital source to combat the severe diseases in the world.[1] World health organization (WHO) reported that the more than 80 % of the world population used the remedies based on plants for their primary health care need.[2,3] The plants are the source for the new drugs, in which the majority are still unexplored. Among the 25 000 000 to 50 000 000 plant species - several percentages of the plants are investigated for their phytochemical and biological screening.[4] India is known for the thousands of species for its medicinal value and the use of the different parts of the plant to cure specific alignment.[5]

Cestrum nocturnum Linn. belongs to Solanaceae. It is commonly known as Raat rani, lady of night or night Jessamine.[6] It contains simple glossy leaves, vine-like stems, greenish-creamy white tubular flowers. The species name 'nocturnum' refers to the species which have the habit of opening its small, heavily-scented flowers at night.[7,8] Hemant Kumar Nagar et al. reported the wound healing activity of *Cestrum nocturnum* (L.) ointment,[9] antidiabetic[10] and antibacterial[11,12] activities.

The present study is done for the investigation of the phytochemicals are occurred in *Cestrum nocturnum* and to determine the physical parameters of its aqueous-extract by different methods. The comparative study was done for conventional extraction (CE) and microwave-assisted extraction (MAE).

Experimental

The plant leaves were collected from the nearby field of Aurangabad city. The leaves were washed gently and dried under shade and were ground. The extraction and analytical methods of phytochemical and physico-chemical parameters like relative density, viscosity, surface tension and refractive index along with phytochemical qualitative tests were carried out as described in our earlier reports.[13-16] The UV-visible spectra were recorded in the range from 190 to 800 nm by using double beam spectrophotometer of Model Elico-159 and λmax values were determined. The FT-IR instrument IRT3000 (JASCO) used to get IR spectra. Antibacterial activity is investigated by cup plate method in which 70 µL of standard test solution was added in each cups or wels and these cups were prepared by using sterile metal borer. The media used was sterile nutrient agar and sterilization was performed in autoclave at 121 ^{0}C for 20 min. For the present study Streptomycine is used as a standard against bacterial culture.

Results and discussion

The leaves of *Cestrum nocturnum* were analyzed to determine their phytochemical, physicochemical and biological properties.

The powder sample is treated with different chemicals and changes in color were registered. The results are shown in Table 1. The solutions gave different colors, for example, concentrated hydrochloric acid gave red while 1 M hydrochloric acid gave creamy color. It can be attributed due to differences in reactivity and color changes according to the pH (indicator property) of different materials are present. The ash content showed the presence of inorganic compounds. The total ash content in the leaves of *Cestrum nocturnum* was found to be 13.4 %. The water-soluble part of the ash was found to be 50 %, while 22 % of the ash does not dissolve even in 1 M hydrochloric acid either.

The summarized properties of the ash made from leaves of *Cestrum nocturnum* are shown in Table 2.

Table 1. Fluorescent test for the leave powder.

Sr. No.	Solutions	Observation
1	The powder as such (P)	Dark green
2	P + n-butanol	Whitish green
3	P + conc. HCl	Red
4	P + conc. HNO_3	Dark orange
5	P + conc. H_2SO_4	Blackish brown
6	P + Ethanol	Whitish green
7	P + Ammonia	Cream
8	P + Glacial acetic acid	Fluorescent green
9	P + 1N HCl	Cream
10	P +1N NaOH	Yellowish green
11	P + 5% HCl	Cream
12	P + 5% NaOH	Yellowish
13	P + benzene	Fluorescent green

Table 2. Ash analysis and densities of leave powder

Sr. No.	Ash	Result
1.	Total ash	13.4 %
2.	Water soluble	50 %
3.	Acid-insoluble	22 %
4.	Bulk density	0.3885 g mL^{-1}
5.	Tab density	0.5018 g mL^{-1}
6.	Housner ratio	1.2916
7.	Carr's index	22.58 %

The leaves of *Cestrum nocturnum* was extracted using the same solvent but different techniques. The difference between conventional extraction (CE) and microwave-assisted extraction (MAE) was registered. The percentages of both extractions were almost the same, but the MAE is more convenient because it gives nearly about the same percentage within half an hour only. The results are shown in Table 3.

Table 3. Extractive value of Cestrum nocturnum leaves

Sr. No.	Solvent	Percentage
1.	Conventional hydrodistillation	24.79
2.	Microwave-assisted hydrodistillation	24.52

Physicochemical properties like density, viscosity, surface tension and refractive index were measured for different concentration of the leave extracts of *Cestrum nocturnum* (Table 4 and 5).

The phytochemical analysis of the plant leaves of both techniques gives the same results (Table 6). This proves that there is no breaking of the compound takes place due to high radiation is the microwave or no breaking takes place due to constant heat in conventional distillation. The test is showing a positive result for alkaloids, carbohydrate, glycoside, saponins, proteins or amino acid phenolic compounds or tannins.

Table 4. Physicochemical properties of CE of leave extract.

Sr. No.	Concentration, ppm	Relative density	Viscosity, Pa s	Surface tension, N m^{-1}	Refractive index
1.	5	0.99758	0.8338	74.8828	0.99970
2.	10	0.99859	0.8346	77.9530	0.99871
3.	20	0.99677	0.8331	74.8230	1.00070
4.	40	0.99677	0.8331	77.8131	1.00070
5.	60	0.99720	0.8335	77.8473	1.00029
6.	80	0.99697	0.8333	74.8380	1.00022
7.	100	0.99556	0.8321	74.7326	1.00176

Table 5. Physicochemical properties of MAE of leave extract.

Sr. No.	Concentration, ppm	Relative density	Viscosity, Pa s	Surface tension, N m^{-1}	Refractive index
1.	5	0.9986	0.8371	50.1188	0.9989
2.	10	1.0037	0.8762	51.6972	0.9936
3.	20	1.0053	0.8779	54.6630	0.9923
4.	40	1.0033	0.8762	54.5551	0.9943
5.	60	1.0054	0.8779	54.6684	0.9922
6.	80	1.0000	0.8733	54.3770	0.9976
7.	100	0.9979	0.8366	59.1979	0.9996

Table 6. Phytochemical analysis of the leave extract of *Cestrum nocuturnum*

Sr. No.	Reagent	CE	MAE
1.	Detection of Alkaloids		
A.	Mayer's test	-ve	-ve
B.	Wagner's test	+ve	+ve
C.	Hager's test	+ve	+ve
2.	Detection of carbohydrate		
A.	Molish test	+ve	+ve
B.	Fehling's test	+ve	+ve
C.	Benedic test	-ve	-ve
D.	Barfoad's test	+ve	+ve
3.	Detection of Glycosides		
A.	Borntrager's test	-ve	-ve
B.	Legal's test	-ve	-ve
4.	Saponins	+ve	+ve
5.	Detection of proteins and amino acid		
A.	Millon's test	+ve	-ve
B.	Nitric acid test	-ve	+ve
C.	Biuret test	+ve	+ve
D.	Ninhydrine test	-ve	-ve
6.	Detection of phenolic compound and tannins		
A.	Ferric chloride test	-ve	-ve
B.	Gelatin test	+ve	+ve
C.	Lead acetate test	+ve	+ve
D.	Alkaline reagent test	+ve	+ve

Spectroscopic results

The IR spectrum of an extract of *Cestrum nocturnum* was also recorded. (ESI Fig.1, Table 7)

Table 7. IR bands of *Cestrum necturnum* plant leaves extract

Band (cm^{-1})	Intensity	Functional group
3329	Very broad	OH (NH) bonds
2942	Sharp	Aliphatic C-H bonds
1609	Sharp	δ(OH)
1417	Broad	C-H bending vibrations
1075	Broad	C-O-C asymmetrical stretching
819	Broad	C-H bands
776	Broad	C-H bands
623	Very broad	aromatic hydrocarbon bands

Though it contains a mixture of compounds but still in order to find out various functional groups and a general fingerprint of samples. The IR bands observed are shown in Table 7. UV spectra of the solutions at ~50 ppm concentration were recorded for both extracts with water as a reference. The spectral data are shown in ESI Fig 2 and Fig 3.

The λ_{max} values were found to be 197 and 248 nm for conventional aqueous extract and microwave assisted aqueous extract, respectively.

Anti-bacterial activity

Both the conventional extraction and microwave-assisted extraction products were tested against E. coli, B. Subtilis and S. Aureus, but antimicrobial activity was found only in the case of CE extract (Table 8). Unfortunately, it does not show any activity against tuberculosis and malaria, while the microwave assisted extract does not show any activity against the listed bacteria trains and tuberculosis or malaria. This may be due to the degradation of compounds which are responsible for the antimicrobial effect.

Table 8. Antibacterial, antituberculosis and antimalarial properties of leaves extract

Sr. No.	Micro-organism	Dead zone diameter, mm		
		MAE	CE	Standard drug
1.	*E. coli*	0	18	12
2.	*B. Subtilis*	0	18	12
3.	*S. Typhi*	0	10	12
4.	*S. Aureus*	0	18	12
5.	T. B	0	0	12
6.	Malaria	0	0	12

Conclusions

The present study revealed that microwave extraction gives the same percent of extraction as the conventional extraction, but the latter is more time-consuming. Both the extract provides the same result for the phytochemicals, including alkaloids, carbohydrates, glycosides, saponins, proteins amino acids, phenolic compounds or tannins content. The conventional extracts showed antibacterial activity against *E. coli*, *B. Subtilis* and *S. Aureus*, while the microwave-assisted extract has no antimicrobial effect due to the degradation of biologically active components.

References

[1]Mohamed Sham Shihabudeen, H., Hansi Priscilla, D, Antimicrobial activity and phytochemical analysis of selected Indian folk medicinal plants, *Int. J.Pharm. Sci. Res. (IJPSR).*, **2010**, *1(10)*, 430.

[2]Rajasekaran, C., Meignanam, E., Vijayakumar, V., Kalaivani, T., Ramya, Y., Premkumar, N., Siva, Y., andJayakumararaj, R., Investigation on antibacterial activity of leaf extract of Azadirachta indica A. Juss (Meliaceae): A traditional medicinal plant of India, *Ethnobotanical Leaflets*, **2008**, *12*, 1213.

[3]Mahesh, B., and Satish, S., Antimicrobial activity of some important medicinal plant against plant and human pathogens *World J. Agricult. Sci*., **2008**, *4(S)*, 839.

[4]Daljit, S. A., Kaur G. J., Antibacterial activity of some medicinal plants, *J. Nat. Med*., **2008**, *61*, 313.

[5]Parekh, J., Jadeja, D., Chanda, S. Efficacy of Aqueous and methanol extract of some medicinal plants for potential antibacterial activity, *Turkey J. Biol*., **2005**, *29*, 203.

[6]Gaurav, M.,. Doshi, Aaditi, S., Mukadam., . Pharmacognostic quantification of flavonoids by high performance thin layer chromatography and in vitro cell line study on developed herbal formulation from Cestrum nocturnum plant extract, *Int. J. Green Pharm*., **2016**, *10(3)*, 183.

[7]Shaista, A., Amrita, P., Delicate, fragrant, lady of the night- A medicinal gift, *J. Med. Plants Studies*, **2016**, *4(6)*, 13.

[8]Al-Reza, S. M., Rahman, A., Ahamd, Y., Kang, S. C., Inhibition of plant pathogans in vitro and in vivo with essential oil and organic extracts of Cestrum nocturnum L, *Pesticide Biochem. Physiol*., **2010**, *96*, 86-92. https://doi.org/10.1016/j.pestbp.2009.09.005

[9]Nagar, H. K., Srivastava, A. K., Srivastava, R., Kumari, M. L., Chandel, H. S., and Ranawat, M. S., Pharmacological investigation of the wound healing activity of Cestrum nocturnum L. ointment in wistar Albino rats, *J. Pharm.*, Article 2016, ID 9249040, 8 pages, https://doi.org/10.1155/2016/9249040

[10]Kamboj, A., Kumar, S. and Kumar, V., Evaluation of antidiabetic activity of hydrochloric extract of Cestrum nocturnum leaves in streptozotocin-induced diabetic rats, *Adv. Pharm. Sci*., **2013**, *1*, 1. http://dx.doi.org/10.1155/2013/150401

[11]Sivaraj, B., Vidya, C., Nandini, S., and Sanil, R., Antimicrobial activity of Cestrum nocturnum L. *Int. J. Curr. Microbiol. Appl. Sci*., **2016**, *4(3)*, 830.

[12]Khan, M. A., Inayat, H., Khan, H., Saeed, M., Khan, I. and Inayat-Ur-Rahman, Antimicrobial activities of the whole plant of Cestrum nocturnum against pathogenic microorganism, *Afr. J. Microbiol. Res*., **2011**, *5(6)*, 612.

[13]Fatema, S., Farooqui, M., Jadhav, S. and Arif, P. M., Phytochemical and physicochemical analysis of conventional and microwave assisted extraction of vitex negundo Linn leaves, *Indo-Amer. J. Pharm. Sci*., **2018**, *5(6)*, 6057.

[14]Fatema, S., Basa'ar, O., Farooqui, M. and Arif, P. M., Phytochemical and physicochemical properties of Hibiscus rosa sinensis leaves extract: A comparison between conventional and microwave assisted extract, *Eur. J. Biomed. Pharm. Sci.*, **2018**, *5(7)*, 551.

15Fatema, S., Parmila, G., Farooqui, M. and Arif, P. M., The phytochemical and antioxidant property of ethereal extract of Hibiscus rosa sinensis leaves extract, *Res. J. Pharm. Biol. Chem. Sci*., **2018**, *9(3)*, 603. https://doi.org/10.20902/ijctr.2018.110821

[16]Basa'ar, O., Fatema, S., Alrabie1, A., Farooqui, M., Supercritical fluid extraction of Cichorium intybus (L) and it's characterization, *J. Chem. Pharm. Sci*., **2016**, *9(4)*, 2936.

This paper was presented at the "*International Symposium on Exploring New Horizons in Chemical Sciences*", January 10–12, 2019, Aurangabad, India (ENHCS–2019).

Received: 23.02.2019.
Accepted: 05.04.2019.

DIFFERENCE BETWEEN RADIOTHERAPY QUALITY ASSURANCE DEVICES (ARC- AND MAP-CHECKS)

T. Gonashvili,[a] K. Kotetishvili,[b] and G. Gavashelishvili[a]

Keywords: QA assurance and control; arc and map-check; oncology; breast and larynx patient; linear accelerator; external beam therapy, intensity-modulated-radiotherapy; volumetric-modulated-arc-therapy; dose distribution and measurement; dosimeters, *c*-index technique; two and three-dimensional plane.

The radiotherapy is a complex procedure and involves understanding of the principles of medical physics, radiobiology, radiation safety, dosimetry, radiation treatment planning, simulation and interaction of radiation with other treatment modalities. Each step in the integrated process of RT needs quality control and quality assurance to prevent errors and to give high confidence that patients will receive the prescribed treatment correctly. A patient-specific quality assurance program has been developed to facilitate the clinical implementation of the intensity-modulated radiotherapy delivered using a micro-multileaf collimator. The methodology includes several dosimetric tasks that are performed prior to the treatment of each patient. Film dosimeter is performed for each individual field and the multifield composite plan. Individual field measurements are performed at a depth of 5 cm in a water equivalent slab phantom. The heterogeneity inserts of phantom are 2 cm×2 cm×22 cm with absorption characteristics of water, brain, muscle, lung, breast, adipose tissue, bone, and liver.

* Corresponding Authors
E-Mail: info@rmc.ge
[a] LIV Hospital, Radiation Medicine Centre, Tbilisi, Georgia
[b] Georgian Technical University, Engineering Physics Department, Tbilisi, Georgia

INTRODUCTION

The purpose of the research is related to the need to develop an analytical approach to planning and question anything different from the norm. This study was conducted to verify planar dose distributions acquired during the pretreatment step of the radiotherapy (RT), in particular, the patient-specific intensity-modulated-radiotherapy (IMRT) quality assurance (QA) delivered at LIV Hospital Radiation Medicine Centre (Tbilisi, Georgia).

EXPERIMENTALS

Our study took one year to provide the appropriate radiation database with clinical conditions: ELEKTA, type of treatment machine, and treatment planning systems (TPS); Treatment approaches: IMRT, S and S IMRT, SBRT, SRS, and volumetric-modulated-arc-therapy (VMAT); QA-devices: Subnuclear, Arc-Check, and Map-Check; Fraction dose: between 1.5–3.0 Gy; and the number of patients: breast – 87 and larynx – 504.

RESULTS AND DISCUSSION

Five hundred ninety-one patient data were evaluated for a time ranging from 2017 to 2018. These data were gauged using several methods used in the QA process. Several patient plan QA in the latter years.

Patients were grouped according to several parameters including TPS, site of treatment, and type of treatment machine used in comparing the measured versus computed dose differences.

With the introduction of advanced RT techniques such as VMAT and IMRT, the three-dimensional (3D) dose distribution for radiation therapy has become both more conformal and complex. These features pose a great challenge for the QA of the dose distribution, which commonly consists of both point dose and two-dimensional (2D) plane dose measurements.[1] And an urgent need for 3D dosimetry has also been stated.[2]

Various techniques have been developed to compare measured dose distributions with those generated by the treatment planning system.[3–24] The *c*-index technique,[3,4] which is the standard method for planar dose verification in IMRT QA,[5,6] calculates the quantity *c* for each point of interest using preselected dose-difference (DD) and distance-to-agreement (DTA) criteria and then uses the *c* value to determine the outcome (pass–fail) of the IMRT QA.

QA measurements are conducted per year for each patient. Quality assurance is specifically defined as the systematic actions necessary to ensure that a product or process performs to specification. The accuracy of each step in the process has a direct impact on treatment outcome.

The following criteria are used for absolute dose and relative dose to determine if a point passes or fails: threshold (TH %), percent difference (Diff %), and distance (Dist, mm). TH % is the minimum dose percent value that must be met in either the device measured or planned dose data for the point to be included in the analysis. Global, so-called Van Dyk, Diff % is the percent difference between the doses at any measured point and the corresponding plan point normalized to a common point (a user-selected normalization point or the maximum dose point – default).

As for the Dist, it is a radius in mm around the measured point. This test refers to points, where the difference between measured and planned values of co-located points exceeds the selected percent difference. Using the distance to agreement criteria, measured point passes if, within a circle of DTA in mm, there exists at least one plan point that is greater than or equal to and at least one plan point that is less than or equal to the value of the measured point. The plot (Table 1) shows all the measurement points that are not in agreement. The points that record a higher value are shown in red (hot) while those that record a lower value are shown in blue (cold).

Table 1. Quality assurance data of breast patients.

Treatment approach	PTV1	PTV2	PTV3	Fraction #	QA Device	Machine	AD Local	AD Global
diMRT	12			6	MapCheck2	Synergy	100	100
diMRT	22			11	MapCheck2	Synergy	95,9	100
diMRT	22			11	MapCheck2	Synergy	98	100
diMRT	69	65	50	37	MapCheck2	Synergy	95,3	99,8
diMRT	14			7	MapCheck2	Synergy	93,8	97,5
diMRT	70	60	54	39	MapCheck2	Synergy	93	100
diMRT	25			9	MapCheck2	Synergy	96,4	99,7
diMRT	27,8	27,8		35	MapCheck2	Synergy	94,6	99,6
diMRT	46			23	MapCheck2	Synergy	98,8	100
diMRT	70	62	56	39	MapCheck2	Synergy	99	100
diMRT	51	54		35	MapCheck2	Synergy	96,6	99,6
diMRT	70	62	58	45	MapCheck2	Synergy	95,6	99,9
diMRT	70	62	58	35	MapCheck2	Synergy	89,7	99,1
diMRT	64			32	MapCheck2	Synergy	100	100
diMRT	22			13	MapCheck2	Synergy	99,7	99,7
diMRT	18			9	MapCheck2	Synergy	100	100
diMRT	70	58		35	MapCheck2	Synergy	99	100
diMRT	70	58		35	MapCheck2	Synergy	97,3	99,5
diMRT	50			25	MapCheck2	Synergy	99,5	100
diMRT	70	55		61	MapCheck2	Synergy	95,1	98,7
diMRT	50			26	MapCheck2	Synergy	98,5	97
diMRT	60			28	MapCheck2	Synergy	94,1	100
diMRT	56			28	MapCheck2	Synergy	93	97,3
diMRT	33			10	MapCheck2	Synergy	99,5	99,7
diMRT	70	58		35	MapCheck2	Synergy	97,1	99,8
diMRT	51			25	MapCheck2	Synergy	97,4	100
diMRT	62	58	54	31	MapCheck2	Synergy	96,2	100
diMRT	28	24		8	MapCheck2	Synergy	100	100
diMRT	70	55		33	MapCheck2	Synergy	93	99,3
diMRT	69			28	MapCheck2	Synergy	100	100
diMRT	70	62	57	35	MapCheck2	Synergy	97,7	99,5
diMRT	50			25	MapCheck2	Synergy	98,5	100
diMRT	45	40		15	MapCheck2	Synergy	99	100
diMRT	58			28	MapCheck2	Synergy	99,7	100
diMRT	63			28	MapCheck2	Synergy	96,4	96,4
diMRT	30			10	MapCheck2	Synergy	93,9	94,8
diMRT	50			25	MapCheck2	Synergy	95,5	100
diMRT	70	60	56	35	MapCheck2	Synergy	88,9	98,2
diMRT	50			25	MapCheck2	Synergy	96	99,4
diMRT	70	60	50	35	MapCheck2	Synergy		
diMRT	70	63	58	35	MapCheck2	Synergy	89,3	93,4
diMRT	70	63	58	35	MapCheck2	Synergy	89,5	99,1
diMRT	70	63	58	35	MapCheck2	Synergy	95,8	99,2
diMRT	40			5	MapCheck2	Synergy	97,7	97,7
diMRT	62	60	54	31	MapCheck2	Synergy	96	100
diMRT	60	58	54	30	MapCheck2	Synergy	97	100
diMRT	70	56		35	MapCheck2	Synergy	92,1	98,3
diMRT	70	62	56	35	MapCheck2	Synergy	98,7	100

Table 2. Quality assurance data of larynx patients

Treatment approach	PTV1	Fraction #	QA Device	Machine	AD Local	AD Global	RD
VMAT	40	10	ArcCheck	Versa HD	89,5	93,6	91,4
VMAT	70	35	ArcCheck	Versa HD	92,2	99,6	100
VMAT	40	35	ArcCheck	Versa HD	96,5	100	100
VMAT	48	24	ArcCheck	Versa HD	99,2	99,9	100
VMAT	26	13	ArcCheck	Versa HD	99,9	100	100
VMAT	24	12	ArcCheck	Versa HD	99,3	100	100
VMAT	70	35	ArcCheck	Versa HD	96	99,8	99,9
VMAT	70	35	ArcCheck	Versa HD	94	99,6	99,7
VMAT	34	17	ArcCheck	Versa HD	99	99,7	99,9
VMAT	70	35	ArcCheck	Versa HD	94,9	99,6	99,9
VMAT	60	30	ArcCheck	Versa HD	80	96,8	97,8
VMAT	32	16	ArcCheck	Versa HD	92,2	97,8	97,4
VMAT	70	35	ArcCheck	Versa HD	97,8	100	100
VMAT	60	28	ArcCheck	Versa HD	98,9	100	100
VMAT	70	34	ArcCheck	Versa HD	91	98,8	99,6
VMAT	70	35	ArcCheck	Versa HD	97,3	99,9	99,9
VMAT	45	25	ArcCheck	Versa HD	97,7	99,8	99,9
VMAT	50	28	ArcCheck	Versa HD	85,3	94,6	97,4
VMAT	60	28	ArcCheck	Versa HD	98,7	100	100
VMAT	60	30	ArcCheck	Versa HD	79	95,4	99,8
VMAT	60	30	ArcCheck	Versa HD	87,7	95,8	98,6
VMAT	42	21	ArcCheck	Versa HD	85,1	96,5	99,2
VMAT	63	28	ArcCheck	Versa HD	92,7	99,6	99,7
VMAT	70	35	ArcCheck	Versa HD	97	100	100
VMAT	50	28	ArcCheck	Versa HD	93,3	98	97,8
VMAT	36	20	ArcCheck	Versa HD	95,1	99,7	99,7
VMAT	18	9	ArcCheck	Versa HD	78,8	92,8	97,4
VMAT	45	15	ArcCheck	Versa HD	93,7	99,3	98,8
VMAT	60	31	ArcCheck	Versa HD	95	98,2	98,6
VMAT	70	35	ArcCheck	Versa HD	96,1	99,6	99,6
VMAT	30	10	ArcCheck	Versa HD	100	100	100
VMAT	30	10	ArcCheck	Versa HD	85,8	94,1	99,4
VMAT	70	35	ArcCheck	Versa HD	90	96,6	
VMAT	70	35	ArcCheck	Versa HD	95,6	99,1	98,8
VMAT	70	35	ArcCheck	Versa HD	97,3	99,8	99,6
VMAT	66	33	ArcCheck	Versa HD	86,1	97,8	97,5
VMAT	70	35	ArcCheck	Versa HD	90,7	95,3	96
VMAT	34	17	ArcCheck	Versa HD	93,9	98	99,1
VMAT	63	28	ArcCheck	Versa HD	89,7	96	95,2
VMAT	62	31	ArcCheck	Versa HD	91,4	99,2	99,4
VMAT	60	30	ArcCheck	Versa HD	93,4	99,4	99,2
VMAT	60	30	ArcCheck	Versa HD	96,2	99,6	99,6
VMAT	70	35	ArcCheck	Versa HD	94,1	98,1	100
VMAT	64	32	ArcCheck	Versa HD	85,6	95,6	99,2
VMAT	30	17	ArcCheck	Versa HD	89,4	95,6	97,7
VMAT	50	25	ArcCheck	Versa HD	94,3	97,1	99,2
VMAT	50	25	ArcCheck	Versa HD	100	100	100
VMAT	70	35	ArcCheck	Versa HD	94,5	99,2	99,3
VMAT	60	30	ArcCheck	Versa HD	70,9	80,4	92,6
VMAT	60	30	ArcCheck	Versa HD	69,4	80,2	92

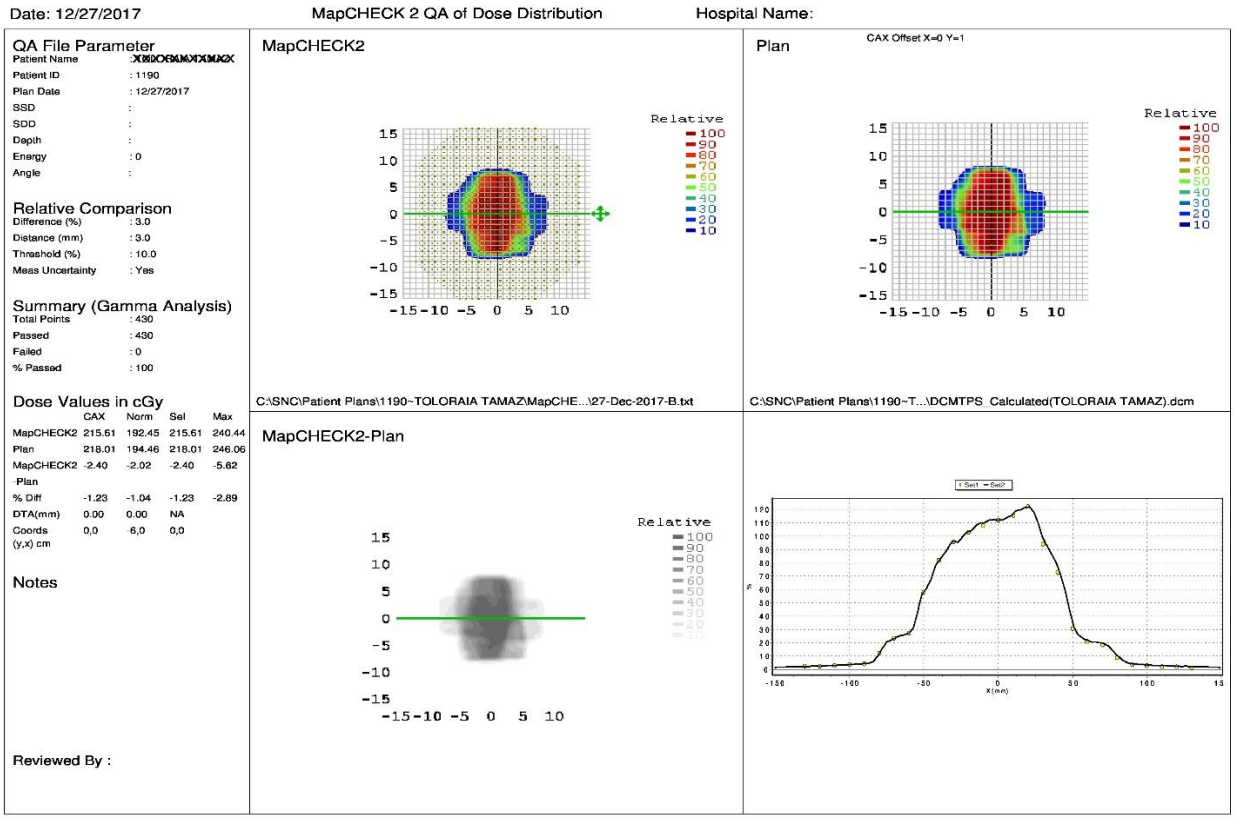

Figure 1. Dose distribution - larynx patient

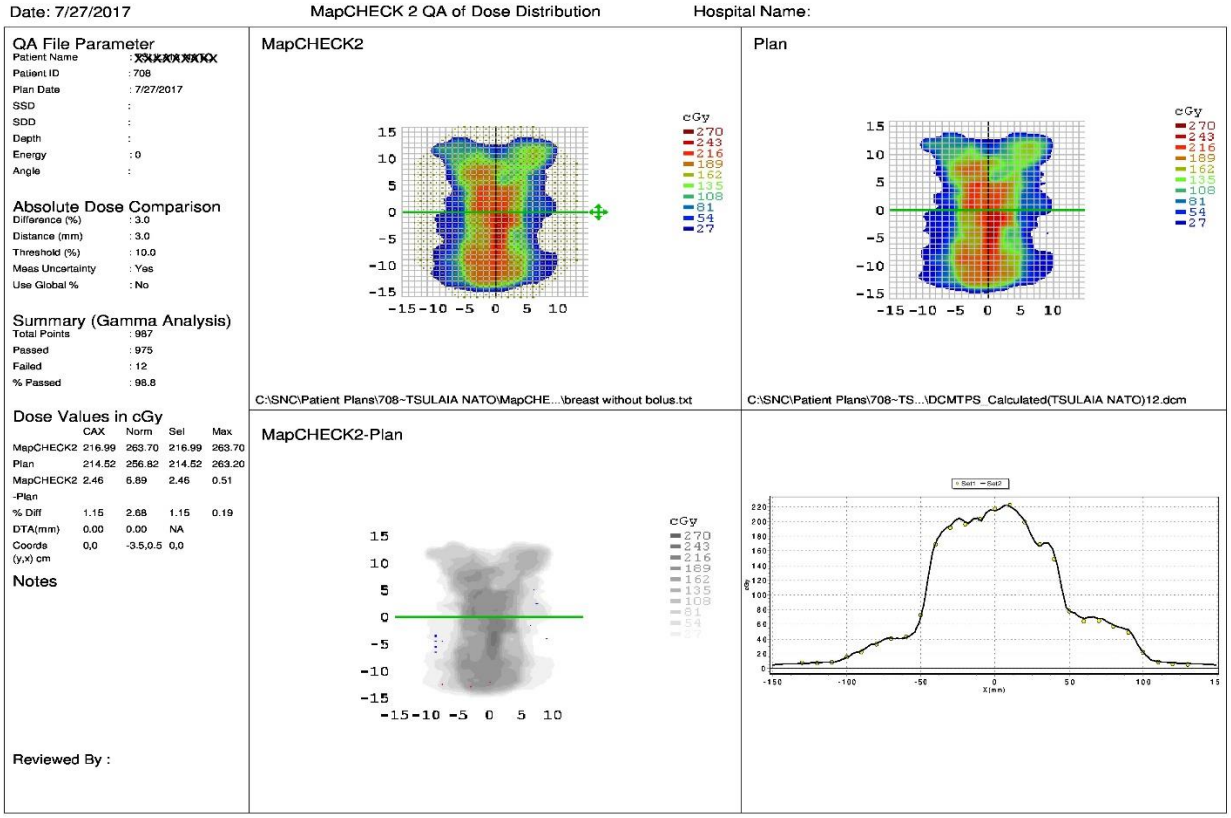

Figure 2. Dose distribution - breast patient

If the Global % checkbox is selected in the analysis panel, the Van Dyk comparison is used during DTA and gamma analysis (Figures 1 and 2).

Global % difference for DTA analysis is defined as the following expression in the SNC patient software:

$$PDE_{k,l} = 100\frac{M_{g,h} - P_{k,l}}{P_{norm}}$$

where:

$PDE_{k,l}$ is the percent dose difference between $M_{g,h}$ and $P_{k,l}$,

$M_{g,h}$ is the measured value at the point (g, h),

$P_{k,l}$ is the planned value at the point (k, l), and

P_{norm} is the planned value at the normalization point.

Global % difference for gamma analysis is defined as the following expression in the SNC patient software:

$$PDE_{k,l} = 100\frac{P_{k,l} - M_{g,h}}{M_{norm}}$$

where:

$PDE_{k,l}$ is the percent dose difference between $M_{g,h}$ and $P_{k,l}$,

$M_{g,h}$ is the measured value at the point (g, h),

$P_{k,l}$ is the planned value at the point (k, l), and

M_{norm} is the measured value at the normalization point.

CONCLUSION

For dose distribution overlays or dose-difference determinations, the results were independent to within a sign of selection of the reference or evaluated distribution. However, for the DTA and γ tools, the results could be profoundly affected by the selection, especially when one or both of the dose distributions contained some noises. Typically, the reference and evaluated distributions would refer to measured and calculated distributions, respectively. But, the final selection should be based on which distribution is considered the standard by which the other is compared.

The γ tool provides a quantitative method for comparing two dose distributions. In this paper, we have shown the utility of the tool to compare two similar dose distributions and evaluated the sensitivity of the tool to pseudorandom noise. In all of these tests, the dose and distance criteria were fixed, preselected values. In practice, the values can be set as functions of space the location of the dose comparison or dose value.

ACKNOWLEDGMENT

Paper was presented at the 5th International Conference "Nanotechnologies", November 19–22, 2018, Tbilisi, Georgia (Nano–2018).

REFERENCES

[1]Bedford, J. L., Nordmark, H. V., McNair, H. A., Aitken, A. H., Brock, J. E., Warrington, A. P., Brada, M., Treatment of lung cancer using volumetric modulated arc therapy and image guidance: A case study. *Acta Oncol.*, **2008**, *47(7)*, 1438-1443. https://doi.org/10.1080/02841860802282778

[2]Otto, K., Volumetric modulated arc therapy: IMRT in a single gantry arc, *Med. Phys.*, **2008**, *35(1)*, 310-317. https://doi.org/10.1118/1.2818738

[3]Feygelman,V.,Zhang,G.,and Stevens, C. Initial dosimetric evaluation of SmartArc - a novel VMAT treatment planning module implemented in a multi-vendor delivery chain**.** *J Appl Clin. Med. Phys.*, **2010**, *11(1)*, 99-116. https://doi.org/10.1120/jacmp.v11i1.3169

[4]Tang. X., Yu, G., Intensity-modulated arc therapy: Principles, Technologies and clinical implementation. *Phys. Med. Biol.*,**2011**, *56(5)*, R31-R54.https://doi.org/10.1088/0031-9155/56/5/r01

[5]Pallotta, S., Marazzo, L., Bucciolini, M., Design and implementation of a water phantom for IMRT, arc therapy, and tomotherapy dose distribution measurements, *Med. Phys.*, **2007**, *34(10)*, 3724-3731. https://doi.org/10.1118/1.2776249

[6]Letourneau, J., Publicover, J., Kozelka, D. J., Moseley, D., Jaffray, A., Novel dosimetric phantom for quality assurance of volumetric modulated arc therapy, *Med. Phys.*, **2009**, *36(5)*, 1813-1821. https://doi.org/10.1118/1.3117563

[7]Gagne, M. W., Ansbacher, S., Zavgorodni, C., Popescu, W. A., Beckham, A., Monte Carlo evaluation of RapidArc dose calculations for oropharynx radiotherapy. *Phys. Med. Biol.*,**2008**,*53(24)*,7167-7185.https://doi.org/10.1088/0031-9155/53/24/011

[8]Korreman, S., Medin, J., Kjaer–Kristoffersen, F., Dosimetric verification of RapidArc treatment delivery. *Acta Oncol.*,**2009**,48(7),185-191.https://doi.org/10.1080/02841860802287116

[9]Verbakel, W., Cuijpers, J.P., Hoffmans, D., Bieker, M., Slotman, B.J., and Senan, S. Volumetric intensity-modulated arc therapy vs. conventional IMRT in head-and-neck cancer: a comparative planning and dosimetric study. *Int. J. Radiat. Oncol. Biol. Phys.*, **2009**, *74(1)*, 252–259. https://doi.org/10.1016/j.ijrobp.2008.12.033

[10]Rao, M., W., Yang, F., Chen, K., Sheng, J., Ye, V., Mehta, D., Shepard, D., Cao. Comparison of Elekta VMAT with helical tomotherapy and fixed field IMRT: Plan quality, delivery efficiency and accuracy. *Med. Phys.*, **2010**, *37(3)*, 1350-1359. https://doi.org/10.1118/1.3326965

[11]Ezzell G. A., Burmeister, J. W., Dogan, N., LoSasso, T. J., Mechalakos, J. G., Mihailidis, D., Molineu, A., Palta, J. R., Ramsey, Ch. R., Shi, J., Xia, P., Yue, N. J., Xiao, Y., IMRT commissioning: multiple institution planning and dosimetry comparisons, a report from AAPM Task Group 119. *Med. Phys.*, **2009**, *36(11)*, 5359-5373. https://doi.org/10.1118/1.3238104

[12]J. O'Daniel, S. Das, Q. J. Wu, F. F. Yin. Volumetric-modulated arc therapy: Effective and efficient end-to-end patient-specific quality assurance. Int. *J. Radiat. Oncol. Biol. Phys.*,**2012**,*82(5)*,1567-1574.https://doi.org/10.1016/j.ijrobp.2011.01.018

[13]Schreibmann, E., Dhabaan, A., Elder, E., Fox, T., Patient-specific quality assurance method for VMAT treatment delivery. *Med. Phys.*, **2009**, *36(10)*, 4530-4535. https://doi.org/10.1118/1.3213085

[14]Zhen, H., Nelms, B. E., Tome, W. A., Moving from gamma passing rates to patient DVH-based QA metrics in pretreatment dose QA, *Med. Phys.*, **2011**, *38(10)*, 5477-5489. https://doi.org/10.1118/1.3633904

[15]Stasi, M., Bresciani, S., Miranti, A., Maggio, A., Sapino, V., Gabriele, P., Pretreatment patient-specific IMRT quality assurance: a correlation study between gamma index and patient clinical dose volume histogram. *Med. Phys.*, **2012**, *39(12)*, 7626-7634. https://doi.org/10.1118/1.4767763

[16]Jin, X., Yi, J., Zhou, Y., Yan, H., Han, C., Xie, C., Comparison of whole field simultaneous integrated boost VMAT and IMRT in the treatment of nasopharyngeal cancer. *Med. Dosim.*, **2013**, *38(4)*, 418-423. https://doi.org/10.1016/j.meddos.2013.05.004

[17] Jin X., Yi, J., Zhou, Y., Yan, H., Han, C, Xie, C., CRT combined with a sequential VMAT boost in the treatment of upper thoracic esophageal cancer. *J. Appl. Clin. Med. Phys.*, **2013**, *14(5)*, 153-161. https://doi.org/10.1120/jacmp.v14i5.4325

[18]Yan G., Lu, B., Kozelka, J., Liu, C., Li, J. G., Calibration of a novel four-dimensional diode array. *Med. Phys.*, **2010**, *37(1)*, 108-115.https://doi.org/10.1118/1.3266769

[19]Nelms, B. E., Opp, D., Robinson, J., Wolf, T. K., Zhang, G., Moros, E., Feygelman, V., VMAT QA: measurement-guided 4D dose reconstruction on a patient. *Med. Phys.*,**2012**, *39(7-1)*, 4228-4238. https://doi.org/10.1118/1.4729709

[20]Bailey, D. W., Nelms, B. E., Attwood, K., Kumaraswamy, L., Podgorsak, M., Statistical variability and confidence intervals for planar dose QA pass rates. *Med. Phys.*, **2011**, *38(11)*, 6053-6064. https://doi.org/10.1118/1.3651695

[21]Nelms, B. E., Zhen, H., Tome, W. A., Per-beam, planar IMRT QA passing rates do not predict clinically relevant patient dose errors. *Med. Phys.*, **2011**, *38(2)*, 1037-1044. https://doi.org/10.1118/1.3544657

[22]Feygelman, V., Opp, D., Zhang, G., Stevens, C., Nelms, B., Experimental verification of the planned dose perturbation algorithm in an anthropomorphic phantom. *J. Phys.Conf. Ser.*, **2013**, *444*, 012047, 4pp. https://doi.org/10.1088/1742-6596/444/1/012047

[23]Carrasco, P., Jornet, N., Latorre, A., Eudaldo, T., Ruiz, A., Ribas, M., 3D DVH-based metric analysis versus per-beam planar analysis in IMRT pretreatment verification. *Med. Phys.*, **2012**, *39(8)*, 5040-5049. https://doi.org/10.1118/1.4736949

Received: 06.01.2019.
Accepted: 11.04.2019.

HIGH DEFORMATIONS IN LEAD SELENIDE NANOLAYERS AND RELATED NEW PROPERTIES

A. M. Pashaev,[a] O. I. Davarashvili,[b]* M. I. Enukashvili,[b] Z. G. Akhvlediani,[b,c] L. P. Bychkova,[b] R.G. Gulayev,[b] M. A. Dzagania,[b,d] and V. P. Zlomanov[e]

Keywords: nanolayers; deformations; dislocations; supercriticality; "negative" pressure.

The article deals with the modified method of "hot-wall" beam epitaxy for obtaining the strained lead selenide nanolayers over a wide range of growth rates and controlling their thickness. With detection of the two-stage growth of the layers, the layers with high deformations – tangential lattice constants, and hence with high "negative" pressure were formed. Observations of the shift of the optical spectrum in strained layers and the possibility of deep compensation of the concentration of current carriers when doping the layers with impurities with variable valence turned out to be interesting as well. Under high deformations, the texture of a tetragonal phase is formed. There appears a new level in the conduction band and hence additional absorption in the optical spectrum. The given specific features were first discovered in the physics and technology of IV–VI semiconductors, and they open new opportunities of using these semiconductors in IR optoelectronics.

* Corresponding Authors
E-Mail: omardavar@yahoo.com
[a] National Aviation Academy of Azerbaijan, Baku, Azerbaijan
[b] I. Javakhishvili Tbilisi State University, Tbilisi, Georgia
[c] E. Andronikashvili Institute of Physics, Tbilisi, Georgia
[d] P. Melikishvili Institute of Physical & Organic Chemistry, Tbilisi, Georgia
[e] M. V. Lomonosov Moscow State University, Moscow, Russia

Introduction

Some new data on the comprehensive research of the strained layers of IV–VI semiconductors have been presented recently.[1] In bulk crystals and thick layers, the atomic number – the weight of the components of the compound determines the chain of interconnected physical properties of IV–VI semiconductors: a narrow band gap leads to small values of effective mass which, in turn, lead to high mobility of current carriers. In thin strained layers, a slight change in the distance between the atoms constituting the compound, for example, with tensile strain is accompanied by an increase in the lattice constant and the band gap, while the mobility of current carriers decreases more significantly than without relaxation of strains at the substrate-layer interface.[2] As the investigation showed, it is important that, when the strained state is retained for two and more years, new opportunities to control smoothly and flexibly the properties of the nanolayers of IV–VI semiconductors and to realize innovative semiconductor device solutions are viewed.[3] Hence the strained nanolayers can be classified as new nanomaterials.

Among the specific features discovered in the strained nanolayers of IV–VI semiconductors, the following ones stand out: supercritical layers under "negative" pressure, non-monotonous dependence of deformations on the growth rate for certain layer thickness, and detection of additional absorption in optical spectra.[4]

From the variety of methods of growing the epitaxial layers of IV–VI semiconductors from liquid and gas phases to obtain single-crystal strained layers, we chose the method of "hot-wall" beam epitaxy.[5–9] In this work, the problems of the growth of the strained layers of IV-VI semiconductors and their discovered physical properties are considered and analyzed by the example of lead selenide.

Technological design and research methods

The method of "hot-wall" beam chosen for growing the strained lead selenide nanolayers is convenient for modification and control of the parameters of the layers. The schematic of the design is shown in Figure 1.

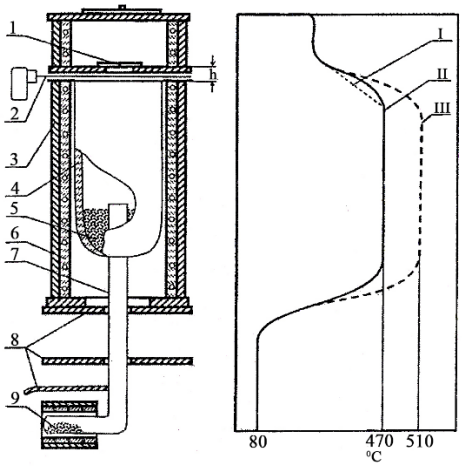

Figure 1. Schematic of design for growing PbSe layers by "hot-wall" beam epitaxy: 1 – substrate, 2 – flapper, 3 – radiation screen, 4 – quartz ampoule, 5 – polycrystals PbSe source, 6 – heater, 7 – tube for selenium vapor, 8 – screen, and 9 – selenium vapor source.

The source of epitaxy–polycrystalline lead selenide (PbSe) was placed on the bottom of a quartz ampoule 19 cm in length and 3.5 cm in diameter. The source was obtained both with the evaporation of a stoichiometric composition and small deviations from stoichiometry (within the homogeneity range) of PbSe in the evacuated system and settled in the zone at 450–510 ºC. The KCl(100), NaCl(100), and BaF_2(111) substrates were prepared by cleavage off immediately before the epitaxy.

Table 1. Layer growth rate control (T_{sub} = 240ºC).

Variant	Source temperature, ºC	Distance between ampoule edge and substrate *h*, mm	Layer growth rate *v*, nm s^{-1}
I	470	12	0.5 – 2
II	470	1	4 – 6
III	510	1	8 – 11

The temperature in the area of the substrate placed on a stainless steel plate varied over the temperature range of 240–310 ºC. The distance between the open edge of the quartz ampoule with the source of epitaxy and the substrate made up 1–20 mm.[10] Results of layer growth rate control are shown in Table 1. Along with the source of epitaxy – PbSe polycrystals with different deviation from stoichiometry, we used an additional selenium source with heating temperature 100–120 ºC to control the type of conduction and the concentration of current carriers.

In the areas of the substrate, the source of epitaxy and the selenium reservoir, the temperature was controlled with an accuracy of 0.3 ºC. The quartz ampoule with a heater with stainless steel casing was placed in a vacuum chamber, where the pressure was kept at $2 \cdot 10^{-6}$ Torr, while the realized growth rates made up 0.1–50 nm s^{-1}. Minimal growth rates were achieved with heating of the substrate from the back side using an incandescent lamp (the temperature gradient was maintained in the thickness of the substrate) and with the distance between the open edge of the quartz ampoule and the substrate of about 20 mm.

The thickness of layers was determined by the X-ray method with the symmetric reflection of the radiation of CoK_α (λ=1.7889 Å) from planes (200) and (400), and determination of the intensity-to-intensity ratio of the radiation reflected from the substrate with a deposited layer and without it. The lattice constant was determined by reflection of radiation from the plane (400) on the relation $a=2\lambda/\sin\theta$, where θ is Bragg's angle.[11] The concentration of current carriers and their mobility at 77 and 300 K were determined by four-probe method.[12,13]

Results and discussion

The growth rate of layers is determined by the rate of delivery of molecules to the substrate. Figure 2 shows the dependences of the thickness *l* of layers on the duration of their growth on KCl(100) substrates with two different distances between the substrate and the open edge of the quartz ampoule with the source I: 2.5 and 12 mm.[14]

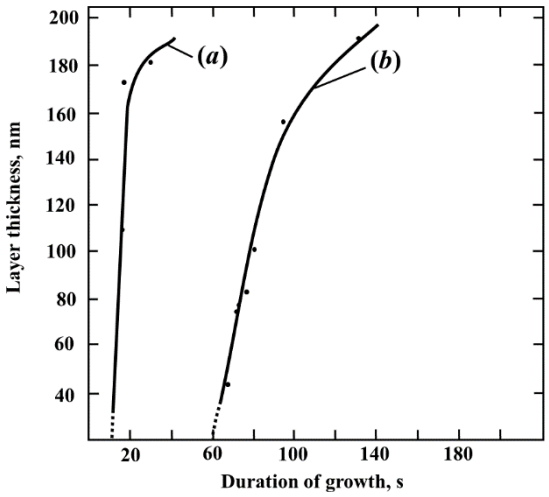

Figure 2. Dependence of thickness of epitaxial PbSe layers on the duration of growth with the distance between the open edge of quartz ampoule and substrate: (a) 1–2.5mm and (b) 1–12mm.

After some time perceived as growth delay t_d, the layers grow faster, especially when *l* = 1mm. It was experimentally determined that, at *1* = 1, 2.5, 12, and 20 mm, the delay time t_d was equal to 2, 9, 60, and 100 s, respectively. Taking into account the sensitivity of the X-ray method – 10 nm, the growth delay can be referred to the time of origination and merging of islets-nuclei. Attributing this event to the first stage of growth, we can conclude that the growth rate in the given cases was equal to 5, 1.1, 0.2 and 0.1 nm s^{-1}, respectively.

At the second stage, the growth rate varies over the range from 0.6 to 50 nm s^{-1}. At the same time, layer-by-layer growth of layers is realized with increasing elastic energy emerging due to a mismatch between the lattice constants of the layer and the substrate: a_{PbSe} = 6.126 and a_{KCl} = 6.290 Å. The indicators of two-stage growth of the layers of IV–VI semiconductors are described in work.[15]

The estimated critical thickness of layers with which elastic energy is transferred to dislocations makes up ≤2nm. As is evident from Table 2, the layers retain the strained state: the lattice constant exceeds 6.126 Å with the thickness of at least >40 nm. This is explained by braking of dislocations when their motion transfers from slip to creep in the result of the location of nonstoichiometric defects in their nuclei, or more precisely annihilation of these defects in dislocations. At the second stage of layer growth, the elastic energy of layers is expanded on the origination and acceleration of dislocations (the relaxation of strain takes place), and from the point of view of achieving maximum defects such a role of dislocations is negative. In contrast, at the first stage, the islets-nuclei flatten faster already with small layer thickness with the relaxation of the surface energy of these islets and their merging occurs, continuous growth of layers accelerates. In this case, loss and transfer of energy to dislocations by nuclei play a positive role.

In Table 2 are given the data on the conditions of growth and the characteristics of layers (temperatures of the substrate and the source, rate of growth, the tangential lattice constant and deformations).

Table 2. Data on conditions of growth and characteristics of strained PbSe layers on KCl(100) substrate.

#	Layer	Temperature, °C		Growth duration, s	Layer thickness, nm	The tangential lattice constant, Å	Layer growth rate, *v*, nm s^{-1}	Relative mismatch–deformation, $\varepsilon = 100(a_I - a_{PbSe})/a_{PbSe}$
		Source	Substrate					
1	SL-541	470	300	80	101	6.162(4)	1.3	0.59
2	SL–558	470	300	77	83	6.172(0)	1.1	0.75
3	SL–555	470	300	75	68	6.177(4)	0.9	0.83
4	SL–562	470	300	67	52	6.188(2)	0.8	1.01
5	SL–215	450	240	300	200	6.129(7)	0.7	0.05
6	SL–578	470	240	30	181	6.249(0)	6.1	0.38
7	SL–283	470	240	13	110	6.144(4)	8.5	0.29
8	SL–284	470	240	15	175	6.136(7)	11.7	0.16
9	SL–602	510	240	12	206	6.139(2)	17.2	0.21
10	SL–605	510	240	20	440	6.132(6)	22.1	0.10
11	SL–623	450	300	130	25	6.202(1)	0.19	1.24
12	SL–177	450	300	330	22	6.219(5)	0.07	1.52

For the first group of layers (SL–541, SL–558, SL–555, and SL–562) grown at l = 12 mm, temperature of the source of epitaxy 470 ºC, and the substrate 280–300 ºC (at which the migration of nonstoichiometric defects raises), low rate of growth <1.5 nm s^{-1}, and thickness of layers <100 nm, the layers grew with high tangential lattice constants reaching 6.190 Å with deformation ~0.01. For the second group of layers (SL–215, SL–578, SL–283, and SL–284) grown at l = 2.5 mm, temperature of the source of epitaxy 470 ºC, and the substrate 300 ºC, and thickness of layers 100–200 nm, the lattice constant did not exceed 6.150 Å, and deformation was <0.003. In the third group of layers (SL–602 and SL–605) grown at l = 1mm, the temperature of the source of epitaxy 510 ºC, and the substrate 240 ºC, the lattice constant was even lower 6.140 Å with deformation <0.002, the thickness of layers was >200 nm.

It should be noted that, by its parameters, layer SL–602 can be referred both to the second and the third groups. The highest tangential lattice parameters were achieved when the substrates were heated from the back side and the distance between the ampoule with the source of epitaxy and the substrate made up 20 mm. At the temperature of the source 450 ºC and the substrate 300 ºC, the tangential lattice constant of the layer, for example, 22 nm thick reached 6.219 Å, and deformation >0.015.

Analyzing the results given in Table 2, we can infer that it is possible to achieve the maximum values of tangential lattice constant by reducing gradually the growth rate of layers, especially when the layer thickness is <100 nm. Really, as the rate of growth of layers by 0.5 nm s^{-1} decreases from 1.3 to 0.8 nm s^{-1}, the tangential lattice parameter increases by 0.030 Å reaching 6.190 Å for the layer 52 nm thick. This occurs due to sufficient location of nonstoichiometric defects in dislocation nuclei. At the same time, at a certain growth rate, the minimal thickness of the layer for the maximum lattice constant can somewhat change with an increase in the density of dislocations in the substrate up to more than 10^6 cm^{-2}.[16,17]

It is noteworthy that the increase in the tangential lattice constant is associated with tensile strain in the layers, and not with the difference between thermal expansion coefficients of the KCl and the PbSe layers, when, on the contrary, the lattice constant of layers decreases. The increase in the lattice constant of layers is connected with the deformations formed at the substrate-layer interface, and not at the boundaries of subgrains – in this case, disorientation is minimal and makes up one hundred-thousandth of a minute.[18]

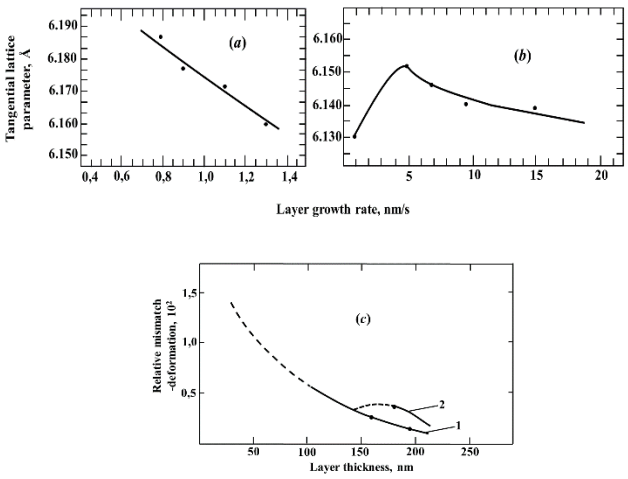

Figure 3. Dependence of tangential lattice parameter of PbSe layers on growth rate with thickness d < 100 nm (a) and d = 100–200 nm (b), and of deformation on the thickness of layers at different growth rates: 1 – 1 and 2 – 6 nm s^{-1} (c).

Figure 3a shows the dependence of the tangential lattice constant on the growth rate of layers for the layers <100nm thick and Figure 3b shows a similar relationship for the layers 100–200 nm thick. In the dependence of the tangential lattice constant on the growth rate, for such a layer, for example, 181 nm thick, there appears the maximum of 6.150 Å at the growth rate of 6nm/s. Apparently with a higher thickness of layers their elastic energy increases, and the relaxation of strains leads to the origination of significantly more dislocations. Bunches of dislocations are formed with their chaotic distribution, and the same number of nonstoichiometric defects is sufficient for formation of clouds limiting the displacement of dislocations. That is why braking of dislocations is more effectively than at low growth rates, when the same concentration of nonstoichiometric defects is

insufficient for application, but, if the density of dislocations is high the investigation of specific features of growth with the thickness of layers 100–200nm is a useful model for achieving high deformations in thinner layers.

At higher growth rates 6 nm $s^{-1} < v < 20$ nm s^{-1}, both for the thickness of layers <100 and 100–200nm, relaxation of strains increases due to the mismatch emerging at the boundaries of subgrains (Figure 3b).[4,19] These conclusions are also illustrated by Figure 3c, which shows the dependence of deformation on the thickness of layers, and that, at the layer thickness of the layer 181 nm, the deformation also increases with the increasing growth rate.

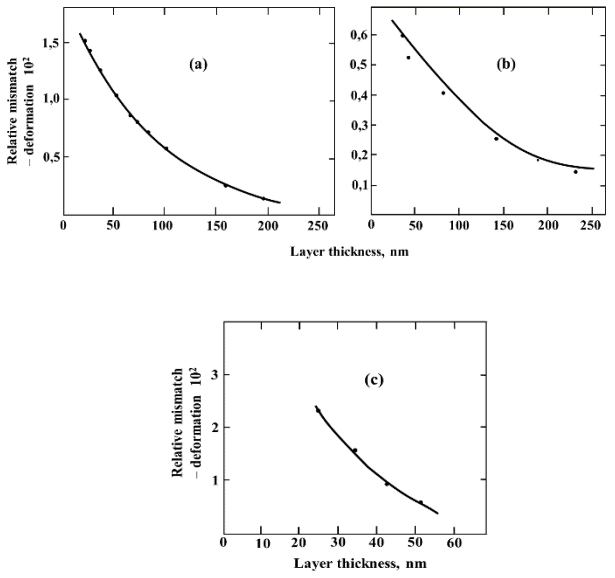

Figure 4. Layer thickness dependence of mismatch – deformation (in relation to single-crystal PbSe) in PbSe layers grown on KCl (a), BaF_2 (b), and NaCl (c) substrates.

A specific role of nonstoichiometric defects with their annihilation in the nuclei of dislocations is manifested with the formation of supercritical layers as well. In Figures 4a, b, and c are shown relative mismatches – deformations in lead selenide layers growing on KCl(100), BaF_2(111), and NaCl(100) substrates depending on the thickness of layers. Comparing the deformations with the thickness 20nm, in the case of KCl (a = 6.290Å), $\varepsilon = 1.5 \cdot 10^{-2}$ and, in the case of BaF_2 (a = 6.200Å), $\varepsilon = 0.6 \cdot 10^{-2}$. In both cases, the deformations of ~0.001 were observed at the thickness of ~200nm. When the layers are grown on the NaCl substrate (a = 5.640Å), due to the higher mismatch in the PbSe layer 20nm thick, the deformation is higher and makes up $\sim 2 \cdot 10^{-2}$, but at the level of ~0.001 it stretches to the thickness of 60nm. In this case, the area of supercriticity reduces because of the compression of layers, while it is significantly larger with stretching – "negative" pressure.

Because of a wide range of tensile strain, it is important to study the "negative" pressure in connection with the possibility of creating a dielectric state with the shift of the impurity level with variable valence deep into the band gap. The impurities of this kind compensate electrically active nonstoichiometric defects and impurity state variables (of different sign).[20]

An additional resource shows up when studying the elastic properties the elastic modulus and critical deformation of PbSe, alloyed with, e.g. chrome, by the method of internal friction. It turned out that the elastic modulus of PbSe increased 3-times, the critical deformation – 2-times, and the elastic limit – 6-times.[21] This allows realizing higher "negative" pressure at the same layer thickness, and hence implementing more deepening of impurity levels into the band gap with stabilization of the Fermi level and more significant compensation off the concentration of current carriers.[22]

Besides the double role of dislocations in the formation of strained lead selenide layers and the determination of the impact of the growth rate on the character of layer growth over a definite range of thickness, an important step is the detection of tetragonal texture in the layers.

In particular, when examining the X-ray diffraction patterns of θ–2θ scanning, it was revealed that, with the thickness of layers from 100 to 300 nm and reflection from planes (200), (400), and (600), there was detected a single band with decreasing intensity as the index h increased. With the thickness of layers less than 100nm, there appears an additional peak, and splitting of X-ray diffraction lines is observed.[4,23]

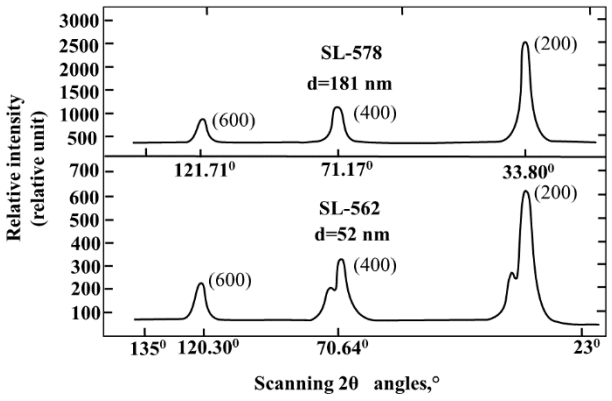

Figure 5. X-ray diffraction patterns of θ–2θ scanning of two PbSe layers with thickness more (SL–577) and less (SL–562) than 100 nm.

Figure 5 shows the X-ray diffraction patterns for layers SL–578 and SL–562 with thicknesses of 181 and 52 nm, respectively. The appearance of texture in the latter case is connected with the formation of a new tetragonal phase with high deformations. The peak on the left in the angular position corresponds to a plane (002). With the increase in the level of deformation, the distance between the basic and the additional peaks increases. Such a peculiarity can be used as calibration for achieving the highest deformations, i.e., high "negative" pressure.

In the scope of systematic studies of optical transmission spectra of the layers of different thickness, the methods of sequential determination of the spectral dependence of refractive indices, and reflection and absorption coefficients.[3,24]

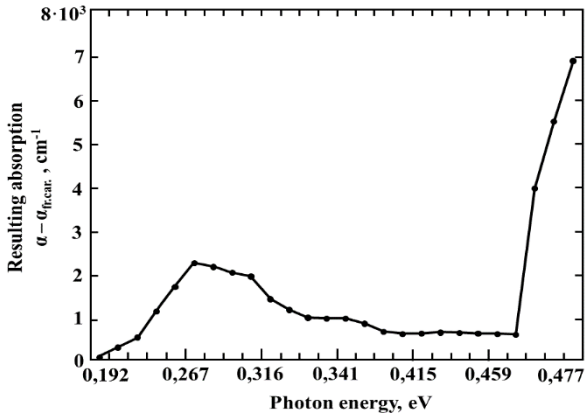

Figure 6. Resulting absorption $\alpha - \alpha_{fr.car.}$ dependence on photon energy.

By straightening of squared absorption coefficients, more exactly of the difference between the total absorption coefficient α and the absorption coefficient for free carriers $\alpha_{fr.car}$.($\alpha - \alpha_{fr.car.}$), the values of lead selenide band gap determined with varying thickness of layers from 4 μm to 70nm varied from 0.286 to 0.465 eV.[2,25] When the texture of the tetragonal phase appears in the X-ray spectrum, a new level emerges in the conduction band. Taking into account the effect of deformation on optical characteristics, in Figure 6 is shown the spectral dependence of $\alpha - \alpha_{fr.car.}$ at 300 K by the example of the lead selenide layer ~70 nm thick. At the concentration of current carriers in the layer of $4 \cdot 10^{18}$ cm^{-3}, additional absorption – a peak in the vicinity of 0.285 eV appears in the optical spectrum.[26]

The increase in the tangential lattice constant and the band gap by 0.055 Å and 0.170 eV, respectively, is an important illustration of the achievement of high deformations, i.e., supercriticity and high "negative" pressure in the layers up to ~10 kbar (with the elastic modulus of $5 \cdot 10^{11}$ dyn cm^{-2}).

Conclusion

Continuous single-crystal strained lead selenide layers 20–500 nm thick with deformation of 0.001-0.02 were grown on the KCl, BaF_2, and NaCl substrates in the "hot-wall" beam epitaxy. The detected two-stage growth of layers and non-monotonous dependence of the tangential lattice constant on the growth rate allowed us to optimize the conditions of formation of "negative" pressure in the layers and to observe a significant shift of the absorption spectra in the strained layers. Due to high deformations, the new texture of the tetragonal phase appears in the strained layers, which is accompanied by the emergence of a new level in the conduction band. The detection of additional absorption in the optical spectrum is connected with this level. By alloying with variable-valence impurities, e.g., chrome, and with the increasing elastic limit, the conditions for more significant shifting of the chrome level to the band gap and more effective compensation of the concentration of current carriers are formed. Innovative effects of the optical spectrum shift, compensation of the concentration of current carriers and detection of additional absorption will serve as a basis for designing high-temperature lasers, photodetectors and modulators of IR radiation based on the studied semiconductors.

Acknowledgment

Paper was presented at the 5th International Conference "Nanotechnologies", November 19–22, 2018, Tbilisi, Georgia (Nano–2018).

References

[1]Pashaev, A. M., Davarashvili, O. I., Enukashvili, M. I., Akhvlediani, Z. G., Bychkova, L. P., Gulyaev, R. G., Dzagania, M. A., Zlomanov, V. P., *Strained semiconductor layers on dielectric substrates (for example: IV–VI materials).* Preprint, **2016**, Tbilisi, ISL–TSU, 22 pp.

[2]Pashaev, A. M., Davarashvili, O. I., Enukashvili, M. I., Akhvlediani, Z. G., Bychkova, L. P., Gulyaev, R. G., Zlomanov. V. P., New analysis of optical parameters of the strained nanolayers of IV–VI semiconductors. *Bull. Acad. Sci. Georgia*, **2017**, *43(3-4)*, 418-426. https://doi.org/10.4028/www.scientific.net/amr.815.473

[3]Pashaev, A. M., Davarashvili, O. I., Enukashvili, M. I., Akhvlediani, Z. G., Bychkova, L. P., Gulyaev, R. G., Dzagania, M. A., Zlomanov, V. P., Investigation of the strained nanolayers of IV–VI semiconductors on dielectric substrates. *Bull. Acad. Sci. Georgia*, **2017**, *43(1)*, 24-36. https://doi.org/10.1088/1757-899x/503/1/012025

[4]Pashaev, A. M., Davarashvili, O. I., Enukashvili, M. I., Akhvlediani, Z. G., Bychkova, L. P., Gulyaev, R. G., Dzagania, M. A., Zlomanov, V. P., Supercritical lead selenide layers at "negative" pressures. *Bull. Acad. Sci. Georgia*, **2017**, *43(2)*, 179-188. https://doi.org/10.1088/1757-899x/503/1/012025

[5]Duh, K., Preier, H., Properties of $PbS_{1-x}Se_x$ epilayers deposited into PbS substrates by "hot -wall" epitaxy. J. Materi. Sci., 1975, 10, 1360-1366.

[6]Kasai, I., Rassett, D. W., Horhung. I., PbSe and $Pb_{0,8}Sn_{0,2}Te$ epitaxial films on cleaved BaF_2 substrates prepared by a modified "hot-wall" technique, *J. Appl. Phys*., **1978,** *47(7)*, 3167-3171. https://doi.org/10.1063/1.323111

[7]Lopez–Otero, A., Hot-wall epitaxy, *Thin Solid Films*, **1978**, *49*, 1-69. https://doi.org/10.1016/0040-6090(78)90309-7

[8]Viatkin, K. V., Shotov, A. P., Ursaki, V. V., Thin layers of $PbS_{1-x}Se_x$, grown by "hot-wall" epitaxy, *Inorg. Mater*., **1981**, *17(1)*, 24-27.

[9]Pashaev, A. M., Davarashvili, O. I., Aliyev, V. A., Gegiadze, G. G., Gulyaev, R. G., Enukashvili, M. I., Zlomanov, V. P., Investigation of thin epitaxial layers of lead selenide. *Georgian Chem. J.*, **2009**, *2(3)*, 201-203. https://doi.org/10.4236/jmp.2012.36068

[10]Pashaev, A. M. Davarashvili, O. I. Enukashvili, M. I. Akhvlediani, Z. G. Bychkova, L. P. Dzagania, M. A. Zlomanov, V. P., Investigation of strained lead selenide nanolayers, *Global J. Eng. Sci. Res. Manag*., **2016**, *3(6)*, 56-64. https://doi.org/10.1088/1757-899x/503/1/012025

[11]Pashaev, A. M., Davarashvili, O. I., Enukashvili, M. I., Bychkova, L. P., Gulyaev, R. G., Dzagania, M. A., Lattice constant as indicator of the technology and the properties of IV–VI semiconductors, *Bull. Acad. Sci. Georgia*, **2017**, *40(2-3)*, 11-16.

[12]Pashaev, A. Davarashvili, O. Akhvlediani, Z. Enukashvili, M. Gulyaev, R. Zlomanov, V., Unrelaxed state in epitaxial heterostructures based on lead selenide, *J. Mod. Phys*., **2012**, *3(6)*, 502-510. https://doi.org/10.4236/jmp.2012.36068

[13]Pashaev, A. M. Davarashvili, O. I. Akhvlediani, Z. G. Enukashvili, M. I. Bychkova, L. P. Dzagania, M. A., Study on the forbidden gap width of strained epitaxial lead selenide layers by optical transmission, *J. Materi. Sci. Eng. B*, **2012**, *2(2)*, 142-150. https://doi.org/10.4028/www.scientific.net/amr.1025-1026.831

[14]Pashaev, A. M. Davarashvili, O. I. Enukashvili, M. I. Akhvlediani, Z. G. Gulyaev, R. G. Bychkova, L. P. Zlomanov, V. P., New studies of growth patterns of lead selenide nanolayers. *Proc. Natl. Acad. Avia. Azerbaijan*, **2012**, *14(4)*, 3-8. https://doi.org/10.4028/www.scientific.net/amr.815.473

[15]Palatnik, L. S. Sorokin, R. K. Zozulya, L. P., The mechanism of growth of isolated particles at epitaxy of lead chalcogenides on NaCl and KCl, *Solid State Phys*., **1969**, *11(5)*, 1265-1270.

[16]Pashaev, A. M. Davarashvili, O. I. Enukashvili, M. I. Akhvlediani, Z. G. Gulyaev, R. G. Dzagania. M. A., Variations of the parameters of PbSe nanolayers with change of their technology. IOP Conf. Ser. Mater. Sci. Eng., **2015**, *77*, 012017, 2-9. https://doi.org/10.1088/1757-899x/77/1/012017

[17]Pashaev, A. M. Davarashvili, O. I. Enukashvili, M. I. Akhvlediani, Z. G. Gulyaev, R. G. Dzagania, M. A., Analysis of growth and properties of epitaxial lead selenide layers in the connection of realization of high "negative" pressure. *Bull. Acad. Sci. Georgia*, **2012**, *38(1)*, 31-35. https://doi.org/10.4236/jmp.2012.36068

[18]Pashaev, A. M., Davarashvili, O. I., Enukashvili, M. I., Akhvlediani, Z. G., Gulyaev, R. G., Bychkova, L. P., Zlomanov, V. P., Stretching strain – effective "negative" pressure in lead selenide nanolayers. Int. J. Eng. & Innov. Technol., **2014**, *3(11)*, 318-323. https://doi.org/10.4028/www.scientific.net/amr.1025-1026.831

[19]Pashaev, A. M., Davarashvili, O. I., Enukashvili, M. I., Akhvlediani, Z. G., Gulyaev, R. G., Bychkova, L. P., Zlomanov, V. P., Modification of the properties of lead selenide layers at their nanothickness, *Nano Studies*, **2013**, *7*, 233-240. https://doi.org/10.4028/www.scientific.net/amr.815.473

[20]Volkov, B. A., Riabova, L. I., Khokhlov, D. R., Impurities with variable valence in the solid solutions on the base of lead telluride. *Usp. Phys*., **2002**, *152*, 1-68.

[21]Pashaev, A. M., Davarashvili, O. I., Aliyev, V. A., Darsavelidze, G. Sh., Enukashvili, M. I., Zlomanov, V. P., Experimental modeling of elastic properties in epitaxial layers of IV–VI semiconductors. *Trans. Natl. Acad. Avia. Azerbaijan*, **2008**, *5*, 96-100.

[22]Pashaev, A. M. Davarashvili, O. I. Enukashvili, M. I. Akhvlediani, Z. G. Gulyaev, R. G. Bychkova, L. P. Zlomanov, V. P., Modeling of quasi-dielectric state in PbSnTe and PbSnSe nanolayers with a high concentration of nonstoichiometric defects. *Nano Studies***,** **2013**, *8*, 253-258. https://doi.org/10.4028/www.scientific.net/amr.815.473

[23]Pashaev, A. M. Davarashvili, O. I. Enukashvili, M. I. Gulyaev, R. G. Dzagania, M. A. Zlomanov, V. P., On the tangential and the normal lattice constants of epitaxial lead selenide layers. *Herald Azerbaijan Eng. Acad*., **2011**, *3(4)*, 13-21. https://doi.org/10.4236/jmp.2012.36068

[24]Pashaev, A. M., Davarashvili, O. I., Enukashvili, M. I., Akhvlediani, Z. G., Bychkova, L. P., Zlomanov, V. P., Study of the optical characteristics of epitaxial $PbS_{1-x}Se_x$ layers. *Global J. Eng. Sci. Res. Manag*., **2016**, *3(2)*, 46-53.

[25]Pashaev, A. M., Davarashvili, O. I., Enukashvili, M. I., Akhvlediani, Z. G., Bychkova, L. P., Zlomanov, V. P., Analysis of the absorption spectra of epitaxial lead telluride and lead selenide layers. *Int. J. Eng. Inn. Technol*., **2015**, *4(11)*, 193-198. https://doi.org/10.4236/jmp.2012.36068

[26]Pashaev, A. M., Davarashvili, O. I., Enukashvili, M. I., Akhvlediani, Z. G., Bychkova, L. P., Dzagania, M. A., Zlomanov, V. P., Additional absorption in the optical spectra of the lead selenide epitaxial layers, *Bull. Acad. Sci. Georgia*, **2014,** *40(4)*, 285-292. https://doi.org/10.4236/jmp.2012.36068

Received: 06.01.2019.
Accepted: 13.04.2019.

SYNTHESIS OF 2-((5-BENZYLIDENE-4-OXO-4,5-DIHYDROTHIAZOL-2-YL)-SUBSTITUTED AMINO ACIDS AS ANTICANCER AND ANTIMICROBIAL AGENTS

Rohini N. Shelke,[a] Dattatraya N. Pansare,*[b]Chandraknat D. Pawar, [c]Mininath C. Khade,[a] Vrushali N. Jadhav,[a]Satish U. Deshmukh, [b] Aniket P. Sarkate, [c]Nileema S. Gore, [e]Rajendra P. Pawar, [b] Devanand B. Shinde, [d] Shankar R. Thopate[a]

Keywords:2-thioxothiazolidin-4-one; Knoevenagel condensation; anticancer activity; antimicrobial activity.

A series of Rhodanine derivatives were synthesized by Knoevenagel condensation. All the synthesized compounds were tested for their in vitro anticancer activity against MCF-7 and BT-474 human breast cancer cell lines. All the synthesized compounds were characterized and screened for their antimicrobial activity against the bacterial and fungal strain. Majority of the compounds showed good to moderate anticancer and antimicrobial activity. Among these compounds, one showed promising activity against gram-positive bacteria *B. subtilis* and *S. aureus* when compared with ampicillin. Some of the most potent compounds possessed selective antimicrobial activity.

*Corresponding Authors
Fax: +91 0240-2400413
E-Mail: dattatraya.pansare7@gmail.com
[a] Department of Chemistry, Prof. John Barnabas Post Graduate School of Biological Studies, Ahmednagar College, Ahmednagar-414001, MS, India
[b] Department of Chemistry, Deogiri college, Station road, Aurangabad-431 005, MS, India.
[c] Department of Chemical Technology, Dr. Babasaheb Ambedkar Marathwada University, Aurangabad-431 004, MS, India.
[d] Shivaji University, Vidyanagar, Kolhapur- 416 004, MS, India.
[e] MGM's Institute of Biosciences & Technology, N-6, Cidco, Aurangabad-431003, MS, India.

INTRODUCTION

The dealing of microbial infections remains a very challenging salutary problem because of emerging infectious diseases and the increasing number of multidrug-resistant microbial pathogens. Even though the many antibiotics, drugs and chemotherapeutic available, the emergence of old and newer antibiotic-resistant bacterial strains in the last two decades created an urgent need for the discovery and development of new antimicrobials with a broader spectrum of activity and lower toxicity.[1-3]

The 2-thioxothiazolidin-4-one (Rhodanine) based molecules exhibit biological activities, such as antidiabetic,[4] anticancer,[5] antitubercular,[6,7] anti-HIV,[8-10] antiparasitic,[11] anticonvulsant,[12] and antiproliferative.[13,14] Thiazole also has anti-inflammatory,[15] anticancer,[16] anti-fungal[17] and anti-microbial[18]activity. The Rhodanine derivatives have been known for over five decades, and there are various reports available on Rhodanine derivatives as antimicrobial agents.[19-24] These reports suggested that Rhodanine nuclei were essential to the observed levels of antimicrobial activity.[25-28]

We make a plan to synthesized Rhodanine derivatives as an antimicrobial agent by preparing hybrid molecules having similar features of reported potent antimicrobial agents (Figure 1).

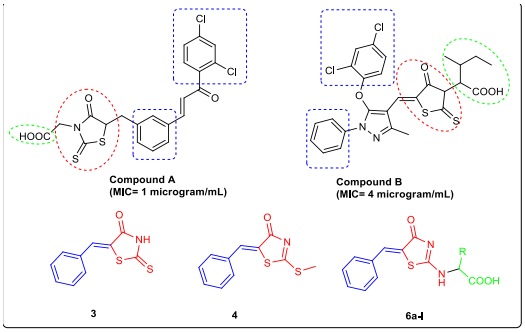

Figure 1. Previously reported antibacterial agents and synthesized compounds.

Because of the facts mentioned above, Rhodanine derivatives were synthesized, characterized by different spectral analysis techniques and screened for their antimicrobial activity. All the synthesized compounds were also screened for their anticancer activity against cell line MCF-7. The results suggest that the compounds could be exploited as an antimicrobial agent. In continuation of our work,[29-42] on the synthesis of heterocyclic and bioactive compounds, we have synthesized some Rhodanine analogs.

MATERIALS AND METHODS

Rhodanine, benzaldehyde and various solvents were commercially available. The major chemicals were purchased from Sigma Aldrich and Avra labs. Reaction courses were monitored by TLC on silica gel precoated F254 Merck plates. Developed plates were examined with UV lamps (254 nm). IR spectra were recorded on an FT-IR (Bruker). Melting points were recorded on SRS Optimelt, melting point apparatus and are uncorrected. The ^{13}C NMR spectra were recorded on a 400 MHz Varian NMR spectrometer. The ^{1}H NMR spectra were recorded on a 400 MHz Varian NMR spectrometer. The chemical shifts are reported as δ (ppm) units (tetramethylsilane). The following

abbreviations are used; singlet (s), doublet (d), triplet (t), quartet (q), multiplet (m) and broad (br). Mass spectra were taken with Micromass-QUATTRO-II of WATER mass spectrometer.

Procedure for the synthesis of (Z)-5-benzylidene-2-thioxothiazolidin-4-one (3)

A mixture of benzaldehyde **1** (1 mmol), 2-thioxothiazolidin-4-one **2** (1 mmol), anhydrous sodium acetate (1 mmol) and glacial acetic acid (1 ml) was refluxed for 5 h. The progress of the reaction was monitored by TLC (20% ethyl acetate: *n*-hexane). After completion of the reaction, the reaction mixture was poured into the ice-cold water. The precipitate was filtered off and washed with water (3×10 ml), dried, and purified by recrystallization in ethanol as a solvent to give 82 % yield.

Orange solid, Yield: 82%. mp 204–206 ºC; ES-MS m/z: 221.05. IR ν_{max}/cm^{-1}: 1670 (C=O), 1600 (C=C), 1585 (C=N), 1230 (C=S), 1192(C–N). ^{1}H NMR: δ (ppm) = 7.40–7.55 (m, 5H, Ar–CH), 7.70 (s, 1H, =CH), 13.90 (s, 1H, NH). ^{13}C NMR: δ(ppm) = 125.5, 128.5, 130.7, 130.9, 131.4, 133.5, 169.4, 194.7.

Procedure for the synthesis of (Z)-5-benzylidene-2-(methylthio)thiazol-4(5H)-one (4)

In a 50 ml round bottom flask, the compound (*Z*)-5-benzylidene-2-thioxothiazolidin-4-one **(3)** (1 mmol), triethylamine (1.2 mmol), iodomethane (1.2 mmol), and dichloromethane (10 ml) were stirred at room temperature for 2 h. The progress of the reaction was monitored by TLC (10% methanol: chloroform). After completion of the reaction, the reaction mixture was concentrated in-vacuo. The residue was washed with water (3×15 mL) to afford the crude product and it was recrystallized from ethanol. Orange solid, Yield: 85%. M.p 145–147 ºC; ES-MS m/z: 235.00. IR ν_{max}/cm^{-1}: 3026 (CH–Ar), 1694 (C=O), 1590 (C=C), 1462 (C=N),1151 (C-S), 979 (C–N). ^{1}H NMR: δ (ppm)= 2.85 (s, 3H, S-CH$_3$), 7.40–7.72 (m, 5H, Ar–CH), 7.90 (s, 1H, =CH). ^{13}C NMR: δ (ppm) = 14.4, 126.5, 128.6, 131.4, 132.9, 133.5, 135.7, 152.3, 162.7, 169.2.

General procedure for the synthesis of (Z)-2-((5-benzylidene-4-oxo-4,5-dihydrothiazol-2-yl)amino) acid (6a-l)

In a 50 ml round bottom flask, the compound **(4)** (1 mmol), amino acids (**5a-l**) (1.2 mmol), potassium carbonate (1 mmol) and ethanol (5 ml) were mixed and stirred for 20-60 min at room temperature. The progress of the reaction was monitored by TLC (10% methanol:chloroform). After completion of the reaction, the reaction mixture was concentrated in-vacuo. The residue was washed with water (3×15 mL) to afford the crude product. The (*Z*)-2-((5-benzylidene-4-oxo-4,5-dihydrothiazol-2-yl) substituted amino acids (**6a-l**) were recrystallized from ethanol and isolated as yellowish solids.

(Z)-2-((5-Benzylidene-4-oxo-4,5-dihydrothiazol-2-yl)amino)propanoic acid (6a).

Yellow solid, Yield: 92%, M.p 221–223 ºC; ES-MS m/z: 277.00. IR ν_{max} /cm^{-1}: 3384 (OH), 3210 (NH), 3026 (CH–Ar), 1737 (HO–C=O), 1599 (C=O), 1553 (C=C), 1599 (C=N), 1006 (C-S), 1091 (C–N). ^{1}H NMR: δ(ppm)= 1.40–1.50 (d, 3H, C–CH$_3$), 4.60–4.70 (q, 1H, CH), 7.40–7.60 (m, 5H, Ar–CH), 7.70 (s, 1H, =CH), 9.15 (s, 1H, NH), 10.20 (s, 1H, COOH). ^{13}C NMR: δ(ppm) = 16.7, 53.4, 127.5, 128.7, 132.7, 135.7, 152.3, 158.6, 167.7, 179.2.

(Z)-2-((5-Benzylidene-4-oxo-4,5-dihydrothiazol-2-yl)amino)-3-methylbutanoic acid (6b).

Yellow solid, Yield: 90%, M.p 178–180 ºC; ES-MS m/z: 304.50. IR ν_{max} /cm^{-1}: 3744 (OH), 3011 (NH), 1737 (HO–C=O), 1689 (C=O), 1553 (C=C), 1509 (C=N), 1232 (C-S), 1010 (C–N). ^{1}H NMR: δ(ppm)= 0.90–0.92 (d, 6H, CH–(CH$_3$)$_2$), 1.52–1.54 (m, 1H, CH), 4.44–4.46 (d, 1H, CH), 7.26–7.68 (m, 5H, Ar–CH), 7.76 (s, 1H, =CH), 9.18 (s, 1H, NH), 10.26 (s, 1H, COOH). ^{13}C NMR: δ(ppm) = 18.7, 30.4, 61.4, 127.9, 128.6, 128.9, 132.3, 135.9, 152.9, 158.1, 167.3, 178.2.

(Z)-2-((5-Benzylidene-4-oxo-4,5-dihydrothiazol-2-yl)amino)-3-methylpentanoic acid (6c).

Yellow solid, Yield: 94%, M.p 110–112 ºC; ES-MS m/z: 319. IR ν_{max}/cm^{-1}: 3365 (OH), 3211 (NH), 3007 (CH–Ar), 1732 (HO–C=O), 1693 (C=O), 1556 (C=C), 1583 (C=N), 1014 (C-S), 1096 (C–N). ^{1}H NMR: δ(ppm)= 0.99–1.01 (t, 3H, CH$_2$–CH$_3$), 1.19–1.22 (d, 3H, CH$_3$) 1.52–1.60 (m, 2H, CH$_2$), 1.81–1.92 (m, 1H, CH), 4.43–4.45 (d, 1H, CH), 7.21–7.62 (m, 5H, Ar–CH), 7.78 (s, 1H, =CH), 9.12 (s, 1H, NH), 11.01 (s, 1H, COOH). ^{13}C NMR: δ(ppm) = 18.7, 30.4, 61.4, 127.9, 128.6, 128.9, 132.3, 135.9, 152.9, 158.1, 167.3, 178.2.

(Z)-2-((5-Benzylidene-4-oxo-4,5-dihydrothiazol-2-yl)amino)-3-phenylpropanoic acid (6d).

Yellow solid, Yield: 92%, M.p 187–189 ºC; ES-MS m/z: 353. IR ν_{max} /cm^{-1}: 3395 (OH), 3213 (NH), 2990 (CH–Ar), 1737 (HO–C=O), 1691 (C=O), 1551 (C=C), 1581 (C=N), 1017 (C-S), 1098 (C–N). ^{1}H NMR: δ(ppm)= 2.51–2.53 (d, 2H, CH$_2$), 4.43–4.78 (q, 1H, CH), 7.21–7.72 (m, 10H, Ar–CH), 7.79 (s, 1H, =CH), 9.14 (s, 1H, NH), 11.02 (s, 1H, COOH). ^{13}C NMR: δ(ppm) = 36.4, 58.4, 125.9, 127.7, 128.6, 128.9, 135.3, 136.9, 152.2, 158.5, 167.1, 175.2.

(Z)-2-((5-Benzylidene-4-oxo-4,5-dihydrothiazol-2-yl)amino)-4-(methylthio)butanoic acid (6e).

Yellow solid, Yield: 90%, M. p 122–124 ºC; ES-MS m/z: 337. IR ν_{max} /cm^{-1}: 3398 (OH), 3200 (NH), 2980 (CH–Ar), 1733 (HO–C=O), 1695 (C=O), 1541 (C=C), 1586 (C=N), 1011 (C-S), 1092 (C–N).

^{1}H NMR: δ(ppm)= 2.01–2.20 (q, 2H, CH_2), 2.20 (s, 3H, CH_3), 2.61–2.63 (t, 2H, CH_2), 4.43–4.78 (q, 1H, CH), 7.31–7.60 (m, 5H, Ar–CH), 7.78 (s, 1H, =CH), 9.16 (s, 1H, NH), 11.22 (s, 1H, COOH). ^{13}C NMR: δ(ppm)=15.4, 29.8, 30.4, 56.4, 127.7, 128.6, 128.9, 132.3, 136.9, 152.2, 158.5, 167.5, 174.9.

(Z)-2-((5-Benzylidene-4-oxo-4,5-dihydrothiazol-2-yl)amino)-4-methylpentanoic acid (6f)

Yellow solid, Yield: 96%, M.p 209–211 ºC; ES-MS m/z: 319. IR ν_{max} /cm^{-1}: 3397 (OH), 3212 (NH), 3013 (CH–Ar), 1734 (HO–C=O), 1691 (C=O), 1555 (C=C), 1583 (C=N), 1013 (C-S), 1091 (C–N). ^{1}H NMR: δ(ppm)= 0.92–0.94 (d, 6H, CH–$(CH_3)_2$), 1.41–1.43 (m, 1H, CH), 1.71–1.73(t, 2H, CH_2), 4.44–4.46 (q, 1H, CH), 7.29–7.69 (m, 5H, Ar–CH), 7.76 (s, 1H, =CH), 9.14 (s, 1H, NH), 10.84 (s, 1H, COOH). ^{13}C NMR: δ(ppm) = 22.7, 24.4, 40.4, 55.2, 127.8, 128.9, 129.2, 132.1, 135.4, 152.2, 159.1, 167.1, 174.2.

(Z)-2-((5-Benzylidene-4-oxo-4,5-dihydrothiazol-2-yl)amino)-3-hydroxypropanoic acid (6g)

Yellow solid, Yield: 95%, M.p 195–197 ºC; ES-MS m/z: 293. IR ν_{max} /cm^{-1}: 3450 (OH), 3214 (NH), 3007 (CH–Ar), 1738 (HO–C=O), 1688 (C=O), 1553 (C=C), 1511 (C=N), 1019 (C-S), 1097 (C–N). ^{1}H NMR: δ(ppm)= 3.60 (s, 1H, CH), 4.01–4.03 (q, 1H, CH), 4.23–4.25 (d, 2H, CH_2),7.31–7.60 (m, 5H, Ar–CH), 7.78 (s, 1H, =CH), 9.12 (s, 1H, NH), 10.86 (s, 1H, COOH). ^{13}C NMR: δ(ppm) = 59.2, 62.3, 127.1, 128.5, 129.2, 132.9, 135.1, 151.9, 158.1, 167.9, 173.2.

(Z)-2-((5-Benzylidene-4-oxo-4,5-dihydrothiazol-2-yl)amino)-3-mercaptopropanoic acid (6h)

Yellow solid, Yield: 92%, M.p 189–191 ºC; ES-MS m/z: 309. IR νmax /cm^{-1}: 3455 (OH), 3201 (NH), 3017 (CH–Ar), 2500 (SH), 1739 (HO–C=O), 1698 (C=O), 1559 (C=C), 1501 (C=N), 1011 (C-S), 1099 (C–N). ^{1}H NMR: δppm= 1.50 (s, 1H, CH), 3.11–3.29 (d, 2H, CH_2), 4.13–4.38 (t, 1H, CH), 7.22–7.59 (m, 5H, Ar–CH), 7.68 (s, 1H, =CH), 9.18 (s, 1H, NH), 11.84 (s, 1H, COOH). ^{13}C NMR: δppm = 26.9, 60.3, 127.5, 128.8, 129.1, 132.5, 135.6, 152.9, 158.3, 167.2, 178.2.

(Z)-2-((5-Benzylidene-4-oxo-4,5-dihydrothiazol-2-yl)-amino)succinic acid (6i)

Yellow solid, Yield: 90%, M.p 169–171 ºC; ES-MS m/z: 321. IR ν_{max} /cm^{-1}: 3465 (OH), 3213 (NH), 3020 (CH–Ar), 1735 (HO–C=O), 1689 (C=O), 1549 (C=C), 1503 (C=N), 1030 (C-S), 1089 (C–N). ^{1}H NMR:δ(ppm)= 2.61–2.63 (d, 2H, CH_2), 3.71–3.73 (t, 1H, CH), 7.33–7.69 (m, 5H, Ar–CH), 7.78 (s, 1H, =CH), 9.30 (s, 1H, NH), 11.74 (s, 2H, COOH). ^{13}C NMR: δ(ppm) = 26.9, 60.3, 127.5, 128.8, 129.1, 132.5, 135.6, 152.9, 158.3, 167.2, 178.2.

(Z)-2-((5-Benzylidene-4-oxo-4,5-dihydrothiazol-2-yl)amino)-3-(1H-imidazol-4-yl) propanoic acid (6j)

Yellow solid, Yield: 94%, M. p 162–164 ºC; ES-MS m/z: 343. IR ν_{max} /cm^{-1}: 3435 (OH), 3215 (NH), 3021 (CH–Ar), 1736 (HO–C=O), 1681 (C=O), 1552 (C=C), 1508 (C=N), 1032 (C-S), 1091 (C–N). ^{1}H NMR: δ(ppm)= 2.91–2.93 (d, 2H, CH_2), 3.72–3.74 (t, 1H, CH), 7.30–7.60 (m, 5H, Ar–CH), 7.64 (s, 1H, =CH), 7.78 (s, 1H, =CH), 8.74 (s, 1H, =CH), 9.30 (s, 1H, NH), 11.74 (s, 1H, COOH), 13.00 (s, 1H, NH). ^{13}C NMR: δ(ppm) = 28.9, 58.3, 117.9,124.7, 127.9, 128.6, 129.2, 132.1, 135.2, 136.7, 152.3, 158.2, 167.5, 176.2.

(Z)-2-((5-benzylidene-4-oxo-4,5-dihydrothiazol-2-yl)amino)-3-(4-hydroxyphenyl) propanoic acid (6k).

Yellow solid, Yield: 93%, mp 192–194 ºC; ES-MS m/z: 369. IR νmax /cm^{-1}: 3465 (O=C-OH), 3395 (OH), 3218 (NH), 2994 (CH–Ar), 1739 (HO–C=O), 1699 (C=O), 1553 (C=C), 1591 (C=N), 1011 (C-S), 1089 (C–N). ^{1}H NMR: δppm= 2.81–2.99 (d, 2H, CH_2), 4.43–4.45(t, 1H, CH), 5.31 (s, 1H, OH),7.30–7.60 (m, 5H, Ar–CH), 7.31–7.72 (m, 4H, Ar–CH), 7.72 (s, 1H, =CH), 9.32 (s, 1H, NH), 11.16 (s, 1H, COOH). ^{13}C NMR: δppm = 36.4, 58.6, 115.9, 127.7, 128.6, 128.9, 129.2, 130.2, 135.3, 136.9, 152.2, 155.7, 158.5, 167.7, 174.2.

(Z)-2-((5-Benzylidene-4-oxo-4,5-dihydrothiazol-2-yl)-amino)-3-hydroxybutanoic acid (6l).

Yellow solid, Yield: 94%, mp 209–211 ºC; ES-MS m/z: 307. IR ν_{max} /cm^{-1}: 3464 (OH), 3202 (NH), 3013 (CH–Ar), 1736 (HO–C=O), 1681 (C=O), 1555 (C=C), 1597 (C=N), 1046 (C-S), 1112 (C–N). ^{1}H NMR: δ(ppm)= 1.15–1.17 (d, 3H, CH_3), 3.52–3.54 (d, 1H, CH), 3.64 (s, 1H, OH), 3.93–4.18 (m, 1H, CH), 7.26–7.68 (m, 5H, Ar–CH), 7.74 (s, 1H, =CH), 9.68 (s, 1H, NH), 11.24 (s, 1H, COOH). ^{13}C NMR: δ(ppm) = 19.7, 64.4, 66.6, 127.8, 128.7, 128.9, 132.4, 135.1, 152.9, 158.2, 167.8, 175.2.

Antimicrobial activity

The antibacterial activity was evaluated against two Gram-positive bacteria namely, *Bacillus subtilis* (NCIM-2063)and*Staphylococcus aureus* (NCIM-2901), and one Gram-negative bacterium *Escherichia coli* (NCIM-2256). The antibacterial activity of compounds was monitored by observing their Minimum Inhibitory Concentration (MIC, μgmL^{-1}) as previously mentionedby the broth dilution method using Ciprofloxacin and Ampicillin as standard drugs. The antifungal activity was evaluated against three fungal strains; *Candida albicans* (NCIM-3471), *Aspergillus flavus* (NCIM-539)and *Aspergillus niger* (NCIM-1196)using Fluconazole and Miconazole as standard drugs. Minimum inhibitory concentration (MIC, μgmL^{-1}) values for antifungal were determined using standard agar dilution method.[43] Methanol was used as solvent control for both antibacterial and antifungal testing. The MIC values of the tested compounds are presented in Table 3.

Anticancer activity

All the synthesized compounds were also tested for their anticancer activity on mammalian cell lines MCF-7 and BT-474 human breast cancer cell line. This test is performed as previously mentioned MTT colorimetric assay.[44] The anticancer activity of the compounds was determined by calculating their IC_{50} values, the concentration of compound

required to inhibit 50% of cell growth compared to untreated control cells. The IC_{50} values were presented in micromol per milliliter (μM). The Adriamycin was used as a positive control for the comparison of the anticancer activity of synthesized compounds.

RESULTS AND DISCUSSION

The synthetic protocols employed for the synthesis of Rhodanine derivatives **3**, **4**, and **6a-l** is presented in Scheme 1. The compound (**3**) was prepared via a Knoevenagel condensation between and benzaldehyde (**1**) andRhodanine (**2**). The compound (**4**) (Scheme 1) was obtained via reaction of the compound (**3**) with iodomethane in dichloromethane using triethylamine as a catalyst.

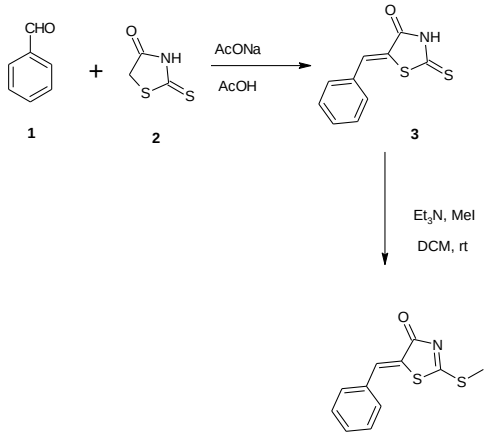

1 2 3

Scheme 1. Synthesis of (*Z*)-5-benzylidene-2-(methylthio)thiazol-4(5H)-one **(4)**

We synthesized and screening of model reaction (*Z*)-2-((5-benzylidene-4-oxo-4,5-dihydrothiazol-2-yl)amino)propanoic acid (**6a**) (Scheme 2, Table 1). The reaction in which the compound **4** (1 mmol) and compound**5a** (1.2 mmol), catalyzed by various bases and various solvents were selected as a model reaction to optimize the reaction conditions. In terms of the effect of solvents and bases on the condensation reaction, potassium carbonate was found to be the better base and ethanol was found to be the best solvent for the reaction (Table 1, entry 11); other solvents, including methanol, acetic acid, N,N-dimethylformamide (DMF) and toluene were less efficient (Table 1, entries 2–5, 7–10 and 12–15).

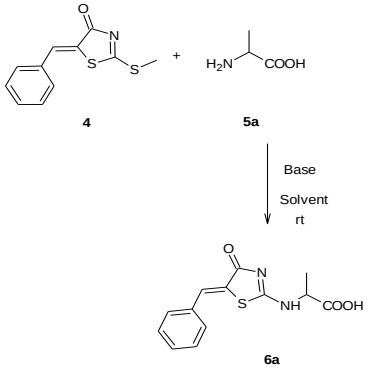

4 5a 6a

Scheme 2 Screening of model reaction (*Z*)-2-((5-benzylidene-4-oxo-4,5-dihydrothiazol-2-yl)amino)propanoic acid (**6a**)[aa]Reaction condition (**6a**). Compound (**4**)(1 mmol), Compound (**5a**)(1.2 mmol), base (1 mmol), solvent 1mL, stirring at rt for 20-80 min.

Table 1. Screening of catalyst, solvents, reaction time, and yield for the synthesis 6a[a].

No.	Base	Solvent	Time, min	Yield,[b] %
1	Et_3N	Ethanol	50	82
2	Et_3N	Methanol	60	65
3	Et_3N	Acetic acid	65	60
4	Et_3N	DMF	70	60
5	Et_3N	Toluene	80	50
6	NaOAc	Ethanol	50	80
7	NaOAc	Methanol	55	50
8	NaOAc	Acetic acid	65	55
9	NaOAc	DMF	70	45
10	NaOAc	Toluene	90	55
11	K_2CO_3	Ethanol	20	98
12	K_2CO_3	Methanol	50	70
13	K_2CO_3	Acetic acid	55	65
14	K_2CO_3	DMF	70	60
15	K_2CO_3	Toluene	80	60

[a]All the reaction was carried out in equimolar amounts of each compound in 1 mL of solvent.[b]Isolated yield.

Nevertheless, all of these yields were best. Ethanol gave the corresponding product in 80–98% yield, which was the best among these solvents (Table 1, entries 1, 6 and 11). To increase the efficiency of the condensation reaction, the effects of different bases were investigated (Table 1, entries 1–15). Potassium carbonate exhibited the best performance with used solvents and gave a better yield, (Table 1, entries 11–15). Sodium acetate and triethylamine gave lower yields with other solvents but gave a better yield in combination with ethanol as a solvent (Table 1, entries 1 and 6). All the reactions were carried out in equimolar amounts of each compound in 1 mL of solvent. Among these reactions, same amounts of the solvent, namely 1 ml of ethanol turned out to be the best choice with yields of 82, 80 and 98% (Table 1, entries 1, 6 and 11). We would like to mention here that ethanol as a solvent with K_2CO_3 as base was the best choice with a yield of 98% and less time required for the completion of the reaction (Table 1, entry 11). Thus we decided to carry out the further reactions in ethanol with potassium carbonate. As a result, the reaction time was shortened; thermal decomposition was also minimized, at room temperature stirring, resulting in higher isolated yields.

Thus we decided the further series, substituted acid derivatives **6a-l**(Scheme 3, Table 2) were synthesized reacting from 5-benzylidene-2-(methylthio)thiazol-4(5H)-one (**4**) with various amino acids (**5a-l**) in ethanol by using K_2CO_3 as a catalyst. In this reaction, there was displacement of a methyl sulfinyl group by amino acids from the C2 position of the thiazolone ring.

The physical data of the synthesized compounds are presented in Table 2. All the reactions proceeded well in 20-60 min to give products in very good yields (82–98%).

The purity of the synthesized compounds was checked by TLC on silica gel precoated F254 Merck plates and melting points were recorded on SRS Optimelt, melting point apparatus and are uncorrected. The structure of the synthesized compounds was confirmed by IR, ^{1}H NMR, ^{13}C NMR and mass spectral analysis.

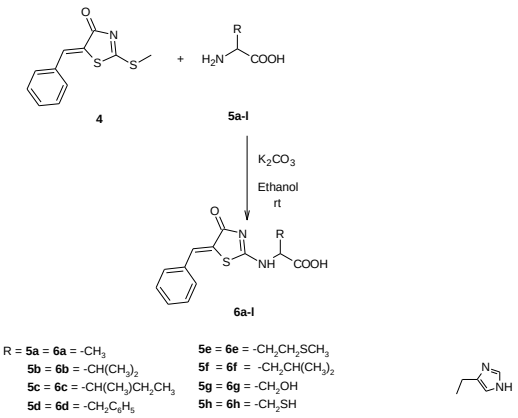

Scheme 3 Synthesis of Z)-2-((5-benzylidene-4-oxo-4,5-dihydrothiazol-2-yl)amino)substituted acid (**6a-l**).

Antimicrobial activity

From the antibacterial activity data (Table 3), the synthesized compounds of present series showed moderate to good antibacterial activity. Amongst the synthesized series, the compounds **6g** (MIC= 15 μgmL^{-1} and 12.5 μg mL^{-1}), **6h** (MIC= 10 μg mL^{-1}and 15 μg mL^{-1})and **6j (**MIC= 6μg mL^{-1}and 5.5 μg mL^{-1})werefound to be most active molecules and they are found to specific towards the Gram-positive bacteria, *S. aureus* and *B. subtilis*. The compound **6j** (MIC= 6.0 and 5.5 μg mL^{-1}against *B. subtilis* and *S. aureus*, respectively) was more active than both standards; Ciprofloxacin (MIC= 6.25 μg mL^{-1}) and Ampicillin (MIC= 12.5 μg mL^{-1}). The compounds **6g** (MIC=15 and 12.5 μg mL^{-1}against *B. subtilis* and *S. aureus*, respectively) and **6h** (MIC= 10 and 15 μg mL^{-1}against *B. subtilis* and *S. aureus*, respectively) showed lower activity thanCiprofloxacin and comparative level of activity as Ampicillin. On the other hand, compound **6f** (MIC= 15μg mL^{-1})was found to be narrow spectrum molecule showing activity only against the bacterium *S. aureus*. Out of these, the remaining compounds of the series **3**, **4**, **6a**, **6i**, **6k**,and **6l** ha**d** very high MIC values and therefore they are inactive as antibacterial agents. It interesting to find out that bacterium *E. coli* is resistance to all compounds, suggest that molecules of the series may be inactive against Gram-negative bacteria.

The results of in vitro antifungal activities showed that synthesized compounds have moderate activity. Most of the synthesized compounds were inactive against fungal strains. Compound **6d** (MIC= 20 μg mL^{-1}) had shown significant activity against *C. albicans* when compared with Miconazole (MIC= 10 μg mL^{-1}). The compounds **4** (MIC= 30 μg mL^{-1}) and **6e** (MIC= 30 μg mL^{-1}) showed moderate activity against *A. niger* when compared with Miconazole (MIC= 6.25 μg mL^{-1}). The compounds **6b** and **6c** (MIC= 25 and 20 μg mL^{-1}against *A. flavus and A. niger*, respectively) were most active from the synthesized series. None of thesynthesized compounds showed comparable activity with that of Fluconazole (MIC= 3.25 μg mL^{-1}).

Anticancer activity

The newly synthesized 14 compounds were screened for their in vitro growth inhibitory activities against two human barest cancer cells line MCF-7 and BT-474, 100 μM (micromol mL^{-1}) by MTT assays method, (Table 4). The results are shown as percentage anticancer activity after 24 h.

The compounds found active in preliminary screening were further studied for their cytotoxic effect on human barest cancer cell line MCF-7 and BT-474 cell lines and the results are expressed as IC_{50}. Among these 14 newly synthesized thiazole derivatives screened for their cytotoxic effect on MCF-7 and BT-474 cells, five compounds showed percentage cell death greater against cell lines used. Among the most active three compounds, two compounds exhibited cell death greater than 50% against both cell lines. The synthesized compounds **6e**, **6f**, **6g**, **6h**, **6k** and **6l** showed maximum percentage cytotoxicity 100 μM.The anticancer studies of compound (**6g**) and (**6l**), against MFC-7 and BT-474 cell lines exhibited IC_{50} values are 1.4, 0.7, 1.2, and 1.3 μM,respectively.

Table 2.Physical data for synthesized Rhodanine derivatives **3**, **4** and **6a-l.**

No.	R	Formula (Mol. wt.)	Time, min	Yield, %	M.P., ºC
3	-	$C_{10}H_7NOS_2$ (221)	300	82	204–206
4	-	$C_{11}H_9NOS_2$ (235)	120	85	145–147
6a	methyl	$C_{13}H_{12}N_2O_3S$ (276)	30	92	221-223
6b	isopropyl	$C_{15}H_{16}N_2O_3S$ (304)	30	90	178-180
6c	sec-butyl	$C_{16}H_{18}N_2O_3S$ (318)	35	94	110-112
6d	benzyl	$C_{19}H_{16}N_2O_3S$ (352)	30	92	187-189
6e	2-(methylthio)ethyl	$C_{15}H_{16}N_2O_3S_2$ (336)	40	90	122-124
6f	isobutyl	$C_{16}H_{18}N_2O_3S$ (318)	50	96	209-211
6g	hydroxymethyl	$C_{13}H_{12}N_2O_4S$ (292)	55	95	195-197
6h	mercaptomethyl	$C_{13}H_{12}N_2O_3S_2$ (308)	50	92	189-191
6i	carboxymethyl	$C_{14}H_{12}N_2O_5S$ (320)	60	90	169-171
6j	imidazoylmethyl	$C_{16}H_{14}N_4O_3S$ (342)	32	94	162-164
6k	4- hydroxybenzyl	$C_{19}H_{16}N_2O_4S$ (368)	40	93	192-194
6l	1-hydroxyethyl	$C_{14}H_{14}N_2O_4S$ (306)	30	94	209-211

The solvent of recrystallization was ethanol; Eluants used in TLC were chloroform: methanol (1:9) for all compounds.

Table 3. In vitro antimicrobial evaluation of synthesizedRhodanine derivatives **3**, **4**, and **6a-l**.

Entry	Antibacterial activity (MIC values in µg mL^{-1})			Antifungal activity (MIC values in µg mL^{-1})		
	B. subtilis	***S. aureus***	***E. coli***	***C. albicans***	***A. flavus***	***A. niger***
3	80	35	100	95	100	100
4	100	100	100	100	95	30
6a	70	60	75	100	80	90
6b	25	15	90	85	25	20
6c	15	20	70	90	25	20
6d	35	30	75	20	90	35
6e	70	100	80	95	35	30
6f	75	15	100	95	70	90
6g	15	12.5	60	95	75	65
6h	10	15	70	65	90	50
6i	100	80	70	95	85	100
6j	6.0	5.5	90	70	85	60
6k	55	65	90	100	80	100
6l	85	100	90	80	95	80
Ciprofloxacin	6.25	6.25	4.0	-	-	-
Ampicillin	12.5	12.5	12.5	-	-	-
Fluconazole	-	-	-	3.25	3.25	3.25
Miconazole	-	-	-	10	6.25	6.25

The data represents the mean values of three replicates; Standard errors were all within 10% of the mean; - denotes not tested.

While the compounds **6e**, **6g**, **6h**, **6k** and **6l** against BT-474 cell lines exhibited IC_{50}: 6.2, 0.7, 6.8, 12.1, and 1.3 µM mL^{-1},respectively. The IC_{50} of reference drug Adriamycin against MFC-7 and BT-474 cells was found to be 0.9 and 0.5 µM mL^{-1},respectively. The anticancer activity of all newly synthesized thiazole derivatives mainly depends on the type of substitution on thiazole moiety. The substitution pattern of amino acids showed variation in anticancer activity.

Table 4.*In vitro*anticancer activity of the studied compounds against the MCF-7 and BT-474cells, after 24 h

Sr. No.	Compounds	IC_{50},[a] µM[b]	
		MCF-7[c]	**BT-474[d]**
1	**3**	68.7	61.3
2	**4**	65.8	62.1
3	**6a**	64.9	42.6
4	**6b**	59.4	63.7
5	**6c**	49.7	66.6
6	**6d**	80.5	42.6
7	**6e**	88.7	6.2
8	**6f**	7.1	55.8
9	**6g**	1.4	0.7
10	**6h**	7.2	6.8
11	**6i**	41.3	74.1
12	**6j**	68.7	64.5
13	**6k**	3.1	12.1
14	**6l**	1.2	1.3
	Adriamycin	0.9	0.5

[a]GI_{50}(Growth inhibition of 50): Concentration of drug that decreases the growth of the cells by 50compared to a non-treated control cell. [b]Values are the average of three readings[c]MCF-7: Human breast cancer cell line[d] BT-474: Human breast cancer cell line[e]Adriamycin: Positive control compound

The compounds with a substituted hydroxyl group attached to thiazole ring which contains amino acids showed the highest percentage of cell death. While the compounds having electron releasing alkyl chain, methyl-1H-imidazole ring group on thiazole rings resulted in the loss of activity.

CONCLUSIONS

We have reported at room temperature, less reaction time with good to excellent yields. All the synthesized compounds were also tested for their *in vitro* anticancer activity against MCF-7 and BT-474 human breast cancer cell lines. Among them most of the compounds show good to excellent anticancer activity, especially **6e, 6f, 6g, 6h, 6k** and **6l** are the most active compounds against tested cell line. The compound **6g** activity value is very close to standard drug, which can be regarded as the promising drug candidate for development of anticancer drugs. The investigation has revealed that a number of Rhodanine derivatives have promising antimicrobial properties.

ACKNOWLEDGMENTS

The authors are thankful to the Head, Department of Chemical Technology, Dr. Babasaheb Ambedkar Marathwada University, Aurangabad 431004 (MS) India, for providing the laboratory facility.

REFERENCES

[1]Azam, F., Alkskas, I.A., Khokra, S.L., Prakash, O., Synthesis of some novel N4-(naphtha[1,2-d]thiazol-2-yl)semicarbazides as potential anticonvulsants, *Eur. J. Med. Chem*., **2009**,*44*, 203. https://doi.org/10.1016/j.ejmech.2008.02.007

[2]Balzarini, J., Orzeszko, B., Maurin, J. K., Orzeszko, A., Synthesis and anti-HIV studies of 2-adamantyl-substituted thiazolidin-4-ones, *Eur. J. Med. Chem.***2007**, *42*, 993. https://doi.org/10.1016/j.ejmech.2007.01.003

[3]Brooke, E. W., Davies, S. G., Mulvaney, A. W., Okada, M., Pompeo, F., Sim, E., Vickers, R. J., Westwood, I. M., Synthesis and in vitro evaluation of novel small molecule inhibitors of bacterial arylamine N-acetyltransferases (NATs), *Bioorg. Med. Chem*.,**2003**,*13*, 2527.https://doi.org/10.1016/S0960-894X(03)00484-0

[4]Murugan, R., Anbazhagan, S., Narayanan, S. S., Synthesis and in vivo antidiabetic activity of novel dispiropyrrolidines through [3+2] cycloaddition reactions with thiazolidinedione and Rhodanine derivatives. *Eur. J. Med. Chem*.,**2009**, *44*, 3272. https://doi.org/10.1016/j.ejmech.2009.03.035

[5]Chandrappa, S., Kavitha, C. V., Shahabuddin, M. S., Vinaya, K., Ananda, C. S., Ranganatha, S. R., Raghavan, S. C., Rangappa, K. S., Synthesis of 2-(5-((5-(4-chlorophenyl)furan-2-yl)methylene)-4-oxo-2-thioxothiazolidin-3-yl)acetic acid derivatives and evaluation of their cytotoxicity and induction of apoptosis in human leukemia cells, *Bioorg. Med. Chem.*, **2009,** *17*, 2576. https://doi.org/10.1016/j.bmc.2009.01.016

[6]Alegaon, S. G., Alagawadi, K. R., Sonkusare, P. V., Chaudhary, S. M., Dadwe, D. H., Shah, A. S., Novel imidazo[2,1-b][1,3,4]thiadiazole carrying Rhodanine-3-acetic acid as potential antitubercular agents, *Bioorg. Med. Chem. Lett*.,**2012**, *22*, 1917. https://doi.org/10.1016/j.bmcl.2012.01.052

[7]Chauhan, K., Sharma, M., Trivedi, P., Chaturvedi, V., Chauhan, P. M. S., New class of methyl tetrazole based hybrid of (Z)-5-benzylidene-2-(piperazin-1-yl)thiazol-4(%H)-one as potent antitubercular agents, *Bioorg. Med. Chem. Lett*., **2014**, *24*, 4166. https://doi.org/10.1016/j.bmcl.2014.07.061

[8]Rajamaki, S., Innitzer, A., Falciani, C., Tintori, C., Christ, F., Witvrouw, M., Debyser, Z., Massa, S., Botta, M., Exploration of novel thiobarbituric acid, Rhodanine and thiohydantoin-based HIV-1 integrase inhibitors, *Bioorg. Med. Chem. Lett*., **2009**, *19*, 3615. https://doi.org/10.1016/j.bmcl.2009.04.132

[9]Murugesan, V., Tiwari, V. S., Saxena, R., Tripathi, R., Paranjape, R., Kulkarni, S., Makwana, N., Suryawanshi, R., Katti, S. B., Lead optimization at C-2 and N-3 positions of thiazolidin-4-ones as HIV-1 non-nucleoside reverse transcriptase inhibitors, *Bioorg. Med. Chem.*, **2011,***19*, 6919.https://doi.org/10.1016/j.bmc.2011.09.018

[10]Kamila, S., Ankati, H., Biehl, E. R., An efficient microwave-assisted synthesis of novel class of Rhodanine derivatives as potential HIV-1 and JSP-1 inhibitors, *Tet. Lett*., **2011**, *52*, 4375. https://doi.org/10.1016/j.tetlet.2011.05.114

[11]Chen, Z. H., Zheng, C. J., Sun, L. P., Piao, H. R., Synthesis of new chalcone derivatives containing a Rhodanine-3-acetic acid moiety with potential anti-bacterial activity, *Eur. J. Med. Chem*., **2010**, *45*, 5739. https://doi.org/10.1016/j.ejmech.2010.09.031

[12]Senthilraja, M., Alagarsamy, V., Solomon, V. R., 2,3-Disubstituted Thiazolidin-4-ones: Novel Class of Anticonvulsant Agents, *Lett. Drug. Des. Dis*. **2012**, *9*, 731.

[13]Ottana, R., Carotti, S., Maccari, R., Landini, I., Chiricosta, G., Caciagli, B., Vigorita, M. G., Mini, E., In vitro antiproliferative activity against human colon cancer cell lines of representative 4-thiazolidinones, *Bioorg. Med. Chem. Lett*.,**2005**, *15*, 3930.https://doi.org/10.1016/j.bmcl.2005.05.093

[14]Gouveia, F. L., de Oliveira, R. M. B., de Oliveira, T. B., da Silva, I. M., do Nascimento, S. C., de Sena, K. X. F. R., de Albuquerque, J. F. C., Synthesis, antimicrobial and cytotoxic activities of some 5-arylidene-4-thioxo-thiazolidine-2-ones. *Eur. J. Med. Chem*.,**2009**, *44*, 2038. https://doi.org/10.1016/j.ejmech.2008.10.006

[15]Sarkate, A. P., Lokwani, D. K., Karnik , K. S., Shinde, D. B., Novel 2-(nitrooxy)ethyl 2-(4-(substituted phenyl)-2-((substituted phenyl)amino)thiazol-5-yl)acetate as anti-inflammatory, analgesic and nitric oxide-releasing agents: Synthesis and Molecular Docking studies, *Anti-Infl. Anti-Allerg. Age. Med. Chem.*, **2017**, *16(3)*, 153-167 https://doi.org/10.2174/1871523016666171115125922

[16]Dofe, V. S., Sarkate, A. P., Azad, R., Gill, C. H., Green synthesis and the inhibitory effect of novel quinoline-based thiazolidinones on the growth of MCF-7 human breast cancer cell line by G2/M cell cycle arrest, *Res. Chem. Intermed.*,**2018**, *44*, 1149. https://doi.org/10.1007/s11164-017-3157-3

[17]Nikalje, A. P. G., Tiwari, S. V., Sarkate, A. P., Karnik, K. S., Imidazole-thiazole coupled derivatives as novel lanosterol 14-α demethylase inhibitors: Ionic liquid-mediated synthesis, biological evaluation and molecular docking study,*Med. Chem. Res*.,**2018**, *27(2)*, 592-606. https://doi.org/10.1007/s00044-017-2085-5

[18]Pawar, C. D., Sarkate, A. P., Karnik, K. S., Bahekar, S. S., Pansare, D. N., Shelke, R. N., Jawale, C. S., Shinde, D. B., Synthesis and antimicrobial evaluation of novel ethyl 2-(2-(4-substituted) acetamido)-4-substituted-thiazole-5-carboxylate derivatives, *Bioorg. Med. Chem. Lett*., **2016**, 26, 3525. https://doi.org/10.1016/j.bmcl.2016.06.030

[19]Gualtieri, M., Bastide, L., Villain-Guillot, P., Michaux-Charachon, S., Latouche, J., Leonetti, J. P., In vitro activity of a new antibacterial Rhodanine derivative against Staphylococcus epidermidis biofilms, *J. Antimicrob. Chemother*,**2006**, *58*, 778. https://doi.org/10.1093/jac/dkl314

[20]Li, H., Yang, J., Ma, S., Qiao, C., Structure-based design of Rhodanine-based acylsulfonamide derivatives as antagonists of the anti-apoptotic Bcl-2 protein, *Bioorg. Med. Chem*.,**2012**, *20*, 4194.https://doi.org/10.1016/j.bmc.2012.05.079

[21]Mallikarjuna, B. P., Sastry, B. S., Suresh Kumar, G. V., Rajendraprasad, Y., Chandrashekar, S. M., Sathisha, K., Synthesis of new 4-isopropylthiazole hydrazide analogs and some derived clubbed triazole, oxadiazole ring systems - A novel class of potential antibacterial, antifungal and antitubercular agents. *Eur. J. Med. Chem*., **2009**, 44, 4739. https://doi.org/10.1016/j.ejmech.2009.06.008

[22]Mueller-Premru, M., Zidar, N., Spik, V. C., Krope, A., Kikelj, D., Benzoxazine, Series of Histidine Kinase Inhibitors as Potential Antimicrobial Agents with Activity against Enterococci, *Chemotherapy*,**2009**, *55*, 414.

[23]Murugan, R., Anbazhagan, S., Lingeshwaran, S., Narayanan, S., Synthesis and in vivo antidiabetic activity of novel dispiropyrrolidines through [3 + 2] cycloaddition reactions with thiazolidinedione and Rhodanine derivatives, *Eur. J. Med. Chem*., **2009**, *44*, 3272. https://doi.org/10.1016/j.ejmech.2009.03.035

[24]Murugesan, V., Tiwari, V. S., Saxena, R., Tripathi, R., Paranjape, R., Kulkarni, S., Makwana, N., Suryawanshi, R., Katti, S. B., Lead optimization at C-2 and N-3 positions of thiazolidin-4-ones as HIV-1 non-nucleoside reverse transcriptase inhibitors, *Bioorg. Med. Chem.*, **2011**,*19*, 6919.https://doi.org/10.1016/j.bmc.2011.09.018

[25]Pansare, D. N., Mulla, N. A., Pawar, C. D., Shende, V. R., Shinde, D. B., One pot three components microwave assisted and conventional synthesis of new 3-(4-chloro-2-hydroxyphenyl)-2-(substituted) thiazolidin-4-one as antimicrobial agents, *Bioorg. Med. Chem. Lett*.,**2014**, *24*, 3569. https://doi.org/10.1016/j.bmcl.2014.05.051

[26]Pansare, D.N., Shelke, R.N., Khade, M. C., Jadhav, V. N., Pawar, C. D., Jadhav, R.A., Bembalkar, S. R., New thiazolone derivatives: design, synthesis, anticancer and antimicrobial activity. *Eur. Chem. Bull.*, **2019**, *8(1)*, 7. DOI: 10.17628/ecb.2019.8.7-14.

[27]Shelke, R.N.,Pansare, D.N., Pawar, C. D.,Khade, M. C., Jadhav, V. N.,Deshmukh, S.U., Dhas, A. K., Chavan, P. N., Sarkate, A. P., Pawar, R. P., Shinde, D. B., Thopate, S.R., Synthesis and anticancer evaluation of new benzenesulfonamide derivatives. *Eur. Chem. Bull*. **2019**, *8(1)*, 1. DOI: 10.17628/ecb.2019.8.1-6.

[28]Petrikaite, V., Tarasevicius, E., Pavilonis, A., New ethacridine derivatives as the potential antifungal and antibacterial preparation, *Medicina*,**2007**, *43*, 657.

[29]Pansare, D. N., Shinde, D. B. A facile synthesis of novel series (Z)-2-((4-oxo-5-(thiophen-2-yl methylene)-4,5-dihydro thiazol-2-yl)amino) substituted acid, *J. Saudi. Chem. Soc*.,**2017**, *21*, 434. https://doi.org/10.1016/j.jscs.2015.10.005

[30]Pansare, D. N., Shelke,R. N., Pawar, C. D., A facile synthesis of (Z)-2-((5-(4-chlorobenzylidene)-4-oxo-4,5-dihydrothiazol-2-yl)amino)substituted acid using microwave irradiation and conventional method, *Lett. Org. Chem.*,**2017**, *14(7)*, 517. https://doi.org/10.2174/1570178614666170524142722

[31]Pansare, D. N., Shelke,R. N., Shinde, D. B., A facial synthesis and anticancer activity of (Z)-2-((5-(4-nitrobenzylidene) -4-oxo-4,5-dihydrothiazol-2-yl)amino) substituted acid, *J. Het. Chem*., **2017**, *54(6)*, 3077. https://doi.org/10.1002/jhet.2919

[32]Pansare, D. N., Shinde, D. B. Synthesis and Antimicrobial Activity of new (Z)-2-((5-(4-Hydroxybenzylidene)-4-Oxo-4,5-Dihydrothiazol-2-Yl)Amino) Acid and its Derivatives, *Res. Rev. J. Chem*.,**2015**, *4(1)*, 1.

[33]Pawar, C. D., Sarkate, A. P., Karnik, K. S., Pansare, D. N., Shinde, D. B., Synthesis and antiproliferative evaluation of new (4-substituted-3,4-dihydro-2H-benzo[b][1,4]oxazin-2-yl)methane substituted sulfonamide derivatives *Eur. J. Chem.*,**2017**, *8*, 384. https://doi.org/10.5155/eurjchem.8.4.384-390.1635

[34]Pawar, C. D., Pansare, D. N., Shinde, D. B., Synthesis of new 3-(substituted phenyl)-N-(2-hydroxy-2-(substituted phenyl)ethyl)-N-methylthiophene-2-sulfonamide derivatives as antiproliferative agents, *Eur. J. Chem.*, **2018**, *9(1)*, 13. https://doi.org/10.5155/eurjchem.9.1.13-21.1669

[35]Pawar, C. D., Pansare, D. N., Shinde, D. B., Synthesis and antiproliferative activity of 3-(substituted)-4,5,6,7-tetrahydro-6-(substituted)-1H-pyrazolo[3,4-c]pyridine Derivatives, *Eur. J. Chem*.,**2017**, *8(4)*, 400-409. https://doi.org/10.5155/eurjchem.8.4.400-409.1645

[36]Shelke,R. N., Pansare, D. N., Pawar, C. D., Pawar, R. P., Bembalkar, S. R., Synthesis of 3H-imidazo[4,5-b] pyridine with evaluation of their anticancer and antimicrobial activity, *Eur. J. Chem*.,**2017**, *8(1)*, 25. https://doi.org/10.5155/eurjchem.8.1.25-32.1522

[37]Shelke,R. N., Pansare, D. N., Pawar, C. D., Deshmukh, A. K., Pawar, R. P., Bembalkar, S. R., Synthesis of 2-((substituted)-2-chloroquinolin-3-yl)-3-((substituted) phenyl) thiazolidin-4-one with β-cyclodextrin-SO_3H catalyst under solvent-free condition, *Res. Rev. J. Chem.*, **2017,** *6(1)*, 24.

[38]Shelke,R. N., Pansare, D. N., Pawar, C. D., Shinde, D. B., Pawar, R. P., Bembalkar, S. R., Synthesis of Novel 2H-Pyrano[2,3-D]Thiazole-6-Carbonitrile Derivatives in Aqueous Medium. *Res. Rev. J. Chem*.,**2016**, *5(2)*, 29.

[39]Sarkate, A. P., Pansare, D. N., Kale, I., Shinde, D. B., Microwave and Conventional Method Assisted Synthesis of 2-(substituted) -3-(4-methoxybenzyl) Thiazolidin-4-ones Using $ZrOCl_2 \cdot 8H_2O$ as a Catalyst. *Curr. Microwave Chem*.,**2017**, *4(2)*, 139-145. https://doi.org/10.2174/2213335603666160922115342

[40]Sarkate, A. P., Pansare, D. N., Kale, I., Bahekar, S. S., Shinde, D. B., Microwave-assisted copper-catalyzed synthesis of substituted benzamides through decarboxylative C-N cross-coupling, *Curr. Microwave Chem.***2017**, *4*, 163.https://doi.org/10.2174/2213335603666161017120230

[41]Pawar, C. D., Pansare, D. N., Shinde, D. B., (Substituted)-benzo[b]thiophene-4-carboxamide synthesis and antiproliferative activity study. *Lett. Drug. Des. Disc*.,**2018**, https://doi.org/10.2174/1570180815666181004114125

[42]Pawar, C. D., Chavan, S. L., Pawar, U. D., Pansare, D. N., Deshmukh, S. V., Shinde, D. B., Synthesis, anti-proliferative activity, SAR and Kinase inhibition studies of thiazol-2-yl-substituted sulfonamide derivatives. *J. Chin. Chem. Soc*.,**2018**, https://doi.org/10.1002/jccs.201800312

[43]Jin, X., Zheng, C. J., Song, M. X., Wu, Y., Sun, L. P., Li, Y. J., Yu, L. J., Piao, H. R., Synthesis and antimicrobial evaluation of L-phenylalanine-derived C5-substituted Rhodanine and chalcone derivatives containing thiobarbituric acid or 2-thioxo-4-thiazolidinone, *Eur. J. Med. Chem*.,**2012**, *56*, 203.https://doi.org/10.1016/j.ejmech.2012.08.026

[44]Denizot, F., Lang, R., Rapid colorimetric assay for cell growth and survival: Modifications to the tetrazolium dye procedure giving improved sensitivity and reliability, *J. Immunol. Met*., **1986**, *89*, 271.

Received: 10.02.2019.
Accepted: 14.04.2019.